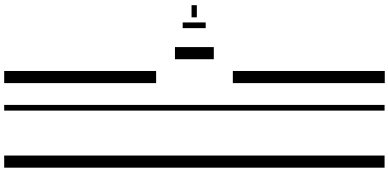

Investigation of Electric Field Effects with the Noble Element Simulation Technique NEST

Bachelor Thesis

Michael Ernst

Westfälische Wilhelms-Universität Münster
Institut für Kernphysik
AG Weinheimer

Referee: Prof. Dr. C. Weinheimer
Co-Referee: Prof. Dr. A. Andronic

Münster, October 2022

Eidesstattliche Erklärung

Hiermit versichere ich, *Michael Ernst*, dass ich die vorliegende Arbeit selbstständig verfasst und keine anderen als die angegebenen Quellen und Hilfsmittel verwendet habe. Gedanklich, inhaltlich oder wörtlich übernommenes habe ich durch Angabe von Herkunft und Text oder Anmerkung belegt bzw. kenntlich gemacht. Dies gilt in gleicher Weise für Bilder, Tabellen, Zeichnungen und Skizzen, die nicht von mir selbst erstellt wurden.

Münster, 27. Oktober 2022

Michael Ernst

Contents

1 Introduction

To this day, only 5 % of our universe's mass-energy content, the baryonic matter, can be described with the standard model of particle physics. Besides the baryonic matter, the universe consists of 25 % dark matter and 70 % dark energy. One candidate for dark matter is the weakly interacting massive particle (WIMP), whose mass is postulated to be in the GeV/c^2 range. With the approach of direct detection of WIMPs the XENON Dark Matter Project is one of the world leading experiments aiming for dark matter detection. Located underground at the Laboratori Nazionali del Gran Sasso (LNGS) in Italy, the latest detector of the experiment, XENONnT, started operating in 2020. In order to search for WIMPS, scattering processes with liquid xenon as a target material are looked at.

The detector technology in XENONnT is the dual-phase time projection chamber (TPC), which allows for high sensitive energy and position reconstructions of detected interactions. Due to an electric drift field inside the TPC, two light signals can be detected per interaction. A prompt scintillation signal and a delayed charge signal, stemming from electrons extracted by the drift field. Therefore, the light and charge signals are affected by the electric field strength. The meta-stable isotope ^{83m}Kr is used as a calibration source in XENONnT. It allows for an internal low energy calibration, as well as spatial corrections of the detected interactions. With its low energetic decay, ^{83m}Kr is used as a basis to form signal correction maps, that account for spatial dependencies in the detected light signal. The detected signal is not only dependent on the geometry of the detector but also on the electric field applied in the TPC.

In this bachelor's thesis the influence of the electric field on the light signals in XENONnT is investigated using the Noble Element Simulation Technique (NEST). The first chapter introduces the XENONnT experiment, contains evidences for dark matter and explains the working principle of TPCs. Signal corrections and the construction of a correction map, as well as the properties of the ^{83m}Kr calibration are described. Furthermore, the electric field simulation which provides a basis for light signal simulations is introduced. The next chapter describes the working principle of NEST and the light signal simulations which depend on the electric field in the TPC. Influences of variations in the electric field and the decay times of ^{83m}Kr on the simulation are analysed. In the following chapter field corrections are calculated

and correction maps are built. A set of correction maps is created by field-corrected signals, another without explicit field correction in the data used. The application of correction maps built from field-corrected signals is supposed not to be limited to interactions of one specific energy. Lastly, corrections freed from influences of the electric field are compared to corrections which do include electric field dependencies. Thus, the applicability of the formed correction maps for specific areas inside the TPC and improvements over correction maps without a field correction in the light signal can be assessed.

2 The XENONnT experiment

There are three main pieces of evidence for the existence of dark matter namely anisotropies in the cosmic microwave background, rotation curves of galaxies and observations via gravitational lensing [10]. Thus, there is a wide variety of motivations for the search of dark matter. In XENONnT, the direct detection method with the dual-phase time projection chamber is used for dark matter detection. This chapter presents observations in rotation curves of galaxies as evidence for dark matter and deals with the detection principle of the TPC. Furthermore, signal correction methods and the usage of the calibration source ^{83m}Kr are explained. Lastly, the electric field simulation of the drift field inside the TPC is covered.

2.1 Evidences for dark matter

As a motivation for the search of dark matter, the rotation curves of galaxies as the oldest evidence for dark matter will be discussed in this section. The circular velocity of galactic objects like gases and stars around the galactic center can be measured using the Doppler effect. These measurements mostly make use of the 21 cm hydrogen transition line [10]. The observed velocity $v(r)$ can be plotted against the distance r from the center of the galaxy as shown in figure 2.1.

According to newtonian dynamics, the velocity decreases with increasing radii:

$$v(r) = \sqrt{\frac{GM(r)}{r}} \tag{2.1}$$

where

$$M(r) = 4\pi \int \rho(r) r^2 dr \tag{2.2}$$

is the mass, G is the gravitational constant and $\rho(r)$ is the mass density profile [10]. It was found that for large radii the rotation curves of many galaxies stay nearly constant, whereas a decline in velocity was expected as indicated by equation 2.1. An additional dark matter halo can explain the differences to the data observed by adding mass to the term $M(r)$, which motivates the search for dark matter.

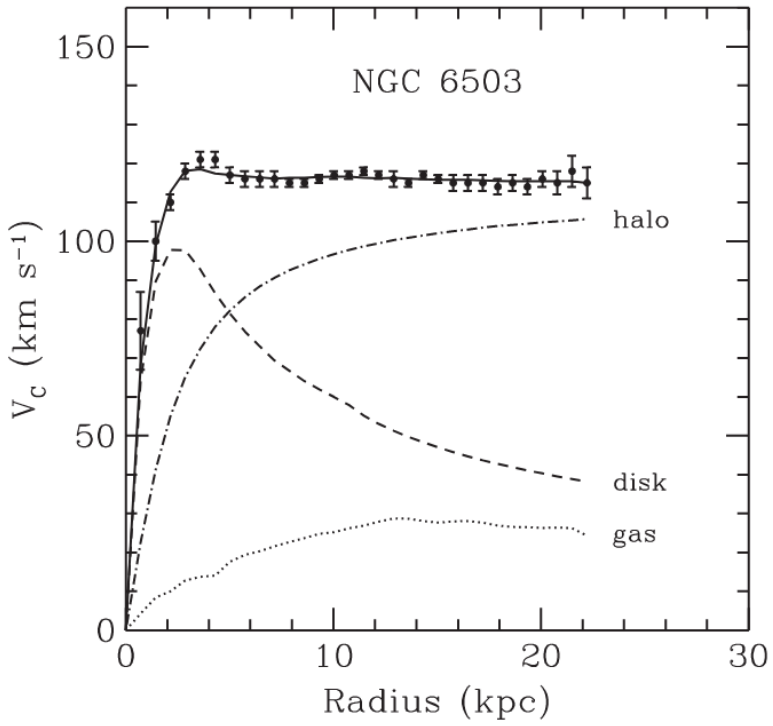

Figure 2.1: Rotation curve of the NGC 6503 galaxy, taken from [9]. The contributions of the gas (dotted), disk (dahed) and dark matter halo (dash-dotted) are additionally shown.

One of the most promising candidates for dark matter is the WIMP, which is predicted to be neutral, stable and weakly interacting. If WIMPs collide with baryonic matter, nuclear recoils (NR) are caused with energies $< 100\,\mathrm{keV}$, which results in excitation and ionisation processes [3]. Thus, scintillation light and free electrons are produced and can be detected through corresponding light signals [3]. The goal of the XENON Dark Matter Project is to observe a WIMP via direct detection methods. Therefore, the next section covers the working principle of time projection chambers.

2.2 The time projection chamber

Since 2005 the XENON Dark Matter Project is established for WIMP search, following the direct detection technique. Located at the LNGS in Italy, the first XENON detector XENON10 was installed holding $\mathcal{O}(10)\,\mathrm{kg}$ of liquid xenon (LXe) as a target mass [11]. The underground location provides the first shielding to cosmic radiation, lowering the experimental background. Using time projection chambers with ultra-low background, the XENON project was able to set world leading limits on the WIMP-nucleon cross section [5]. With its successors XENON100 in 2008 and XENON1T in 2016 the low background and sensitivity of

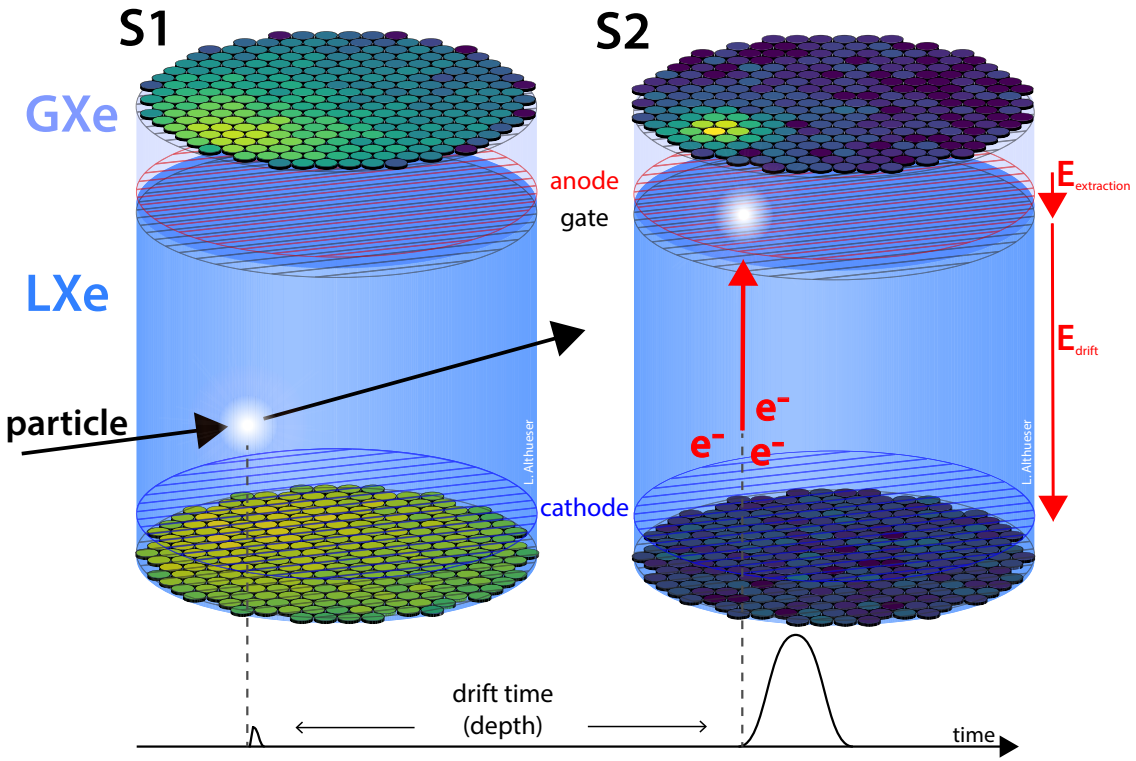

Figure 2.2: Schematic view of the TPC taken from [16]. Left: S1 is observed by both PMT arrays after an incoming particle interacts with LXe. Right: Through the drift field E_{drift} electrons are pulled towards the GXe phase where S2 is produced.

direct dark matter search was improved. In the year 2020 the latest detector XENONnT was installed and took its first science run in 2021. Today, more than 180 scientists from 11 countries collaborate in the XENONnT experiment for the search of dark matter [11].

At the centre of the setup stands the TPC, filled with an active mass of 5.9 tonnes of liquid xenon [8]. It has a diameter of 1.33 m and a height of 1.49 m with a radially symmetric cylindrical shape. At the bottom and top two arrays of photomultiplier tubes (PMTs) are installed for scintillation light detection. The top array holds 253 PMTs and the bottom array 241 PMTs. Figure 2.2 shows the working principle of the TPC. It consists of a LXe phase at the bottom and a gaseous phase (GXe) at the top. An electric drift field inside the TPC is generated by a cathode at the bottom and an anode at the top. Below the GXe phase, a grounded gate mesh allows for a stronger extraction field in this phase. The positions of anode and gate electrode are 3 mm above and 5 mm below the liquid-gas interface [8]. All electrodes consist of stainless steel wires with a diameter of 216 µm, except the cathode electrode with a diameter of 304 µm [8]. In addition, perpendicular wires are installed at the anode and gate to prevent the electrodes from bending. The cathode electrode is placed 1485 mm below the gate electrode. Additionally, two screening electrodes are placed below the top PMT array

and above the bottom PMT array to protect them from high electric fields. Furthermore, the TPC is surrounded by a field cage, which consists of copper field shaping rings (FSR) in order to obtain the uniformity of the drift field [7]. Therefore, two concentric sets of vertically interleaved copper field shaping elements are placed at the edges of the TPC. While the field shaping rings prevent the electric field from high variations, homogeneity of the drift field is assumed. Because the field strength can not be measured directly, the local field strength has to be reconstructed from calibration data or has to be simulated, which is explained in section 2.5. The rings form the field cage and consist of 71 field shaping wires in the inner set and 64 guards, which are placed 1 cm outwards from the wires. The TPC is surrounded by a water tank, which holds the neutron veto system (nVeto) and the muon veto system (μVeto). They provide methods for passive shielding and the reduction of nuclear recoil backgrounds.

With the high charge number Z of the heavy noble gas xenon ($Z = 54$) and its high atomic number A ($A = 124$ to $A = 136$), LXe is a suitable target material for dark matter search [3], because weak interaction rates are proportional to A^2. Furthermore, the high density of LXe of roughly $3\,\mathrm{g/cm^2}$ leads to self-shielding abilities, which can reduce the background of the experiment [6]. If a particle scatters with LXe in the TPC, excitation and ionization of xenon atoms occur via nuclear recoil interactions with the xenon nucleus, or electronic recoil interactions (ER) with electrons from the atomic shell. In both cases, free electrons and scintillation light is produced. The scintillation light has a wavelength of 178 nm [3]. It has the same wavelength for processes of electron-ion recombination (equation 2.3) and direct excitation (equation 2.4). Both processes can produce scintillation light in xenon and are shown in the following equations [3]:

$$\begin{aligned}
\chi + \mathrm{Xe} &\rightarrow \mathrm{Xe}^+ + e^- + \chi \\
\mathrm{Xe}^+ + \mathrm{Xe} &\rightarrow \mathrm{Xe}_2^+ \\
\mathrm{Xe}_2^+ + e^- &\rightarrow \mathrm{Xe}^{**} + \mathrm{Xe} \\
\mathrm{Xe}^{**} &\rightarrow \mathrm{Xe}^* + \mathrm{heat} \\
\mathrm{Xe}^* + \mathrm{Xe} + \mathrm{Xe} &\rightarrow \mathrm{Xe}_2^* + \mathrm{Xe} \\
\mathrm{Xe}_2^* &\rightarrow 2\mathrm{Xe} + h\nu
\end{aligned} \tag{2.3}$$

$$\begin{aligned}
\chi + \mathrm{Xe} &\rightarrow \mathrm{Xe}^* + \chi \\
\mathrm{Xe}^* + \mathrm{Xe} + \mathrm{Xe} &\rightarrow \mathrm{Xe}_2^* + \mathrm{Xe} \\
\mathrm{Xe}_2^* &\rightarrow 2\mathrm{Xe} + h\nu
\end{aligned} \tag{2.4}$$

In both cases, an excited xenon dimer is created that generates a prompt scintillation signal through de-excitation. This prompt scintillation signal is called S1 and is measured by the PMTs. The size of S1 is reported in the number of photoelectrons (PE). Because of the reflections by the liquid-gas interface and the polytetrafluoroethylene (PTFE) panels at the TPC walls, S1 is mainly detected by the bottom PMT array. The free ionisation electrons that do not recombine with xenon atoms are drawn to the GXe phase by the drift field. As the electrons pass the gate, they are extracted by the stronger extraction field into the GXe phase. This results in a second proportional scintillation signal, called S2. The strength of the drift field influences the number of electrons, recombining with the ionised xenon dimers and leads to an anti-correlation of S1 and S2 signals. S1 and S2 can be classified by their different time width. The discrimination of nuclear and electronic recoils is important, because WIMPs will scatter via NR interactions instead of ER interactions. As the ionisation density differs for ER and NR interactions the ratio of S1 and S2 can be used for discrimination of those.

One of the main advantages of dual-phase TPCs is the position reconstruction of signals. The accurate reconstruction can be used for the exclusion of background events and for signal corrections [5]. The position reconstruction for an interaction in the TPC uses the time difference between S1 and S2 for reconstructing the z-coordinates. With the knowledge of the electric field also the constant but field dependent drift velocity of electrons can be calculated. Using this information and the time difference between S1 and S2, the depth of the signal in z-direction can be reconstructed. For the x- and y-position reconstruction in the horizontal plane, the light distribution of S2 signals on the top PMT array is used [8].

2.3 Signal corrections

The light signal S1 and charge signal S2 both have to be corrected for multiple position dependent effects. This thesis mainly deals with S1 signals and therefore focuses on S1 correction methods. For S2 corrections, an electron lifetime correction and a spatial correction are applied [6]. Not all scintillation light produced is present in S1, because of position dependent effects in the TPC, such as electron attachment to impurities, field inhomogeneities and variations of thickness of the proportional scintillation region [6]. This indicates that the measured light yield (LY) gets smaller, due to impurities or absorbtions from the walls in the TPC. The light yield is dependent on the position of the interaction and defined as S1 signal per incident energy E [6]:

$$\frac{S1(R,\phi,z,E,F)}{E} = LY(R,\phi,z,E,F) = \epsilon_L(R,\phi,z) \cdot PY(E,F) \cdot \epsilon_{QE} \cdot \epsilon_{CE} \ . \tag{2.5}$$

The light yield can also be calculated by the product written on the right hand side of equation 2.5, including following factors:

- Photon Yield (PY(E,F)): The number of generated photons per energy E. The drift field $F = F(R, \phi, z, t)$ is generally position dependent. For the number of generated electrons per energy, the term quantum yield (QY(E,F)) is used.

- Light Collection Efficiency ($\epsilon_L(R, \phi, z)$): The number of photons that hit a PMT per emitted photon. ϵ_L is position dependent because the photon that hits a PMT can be reflected in the TPC.

- Quantum Efficiency (ϵ_{QE}): The probability that a PE is generated at the cathode by an incoming photon.

- Collection Efficiency (ϵ_{CE}): The probability of one PE being collected at the PMT dynodes.

For ϵ_{QE} and ϵ_{CE}, constant values are assumed that only rely on the characteristics of the PMT. The equivalent yield for the charge signal S2 is called charge yield (CY). In order to correct the geometrical effects, a correction map of the relative light collection efficiency (LCE) is formed. This map corrects S1 signals dependent on their position in the TPC and should result in a nearly constant, corrected S1. In general, both the light collection efficiency ϵ_L and the electric field F are position dependent. Only in the case of a constant energy and a constant field strength, the averaged value of PY can be separated from ϵ_L.

For this purpose, the S1 signal is arranged in bins and a mean value of S1 is calculated for each bin. A bin is a small volume inside the TPC and the bin sizes are chosen as follows:

- z: In z-direction, the TPC volume is divided into 45 parts. These z-slices span from $-148.5\,\text{cm}$ to $0\,\text{cm}$ in height with an interval of $3.3\,\text{cm}$ for each slice.

- r: The radial division is evenly spaced in r from $0\,\text{cm}$ to $66.5\,\text{cm}$ in 6 annular segments, called rings.

- ϕ: The number of bins in ϕ-direction is increasing with each ring. For the number of bins n_b per annular segment N_r the equation

$$n_b = 2 \cdot N_r - 1 \tag{2.6}$$

  is used. This ensures a constant volume for each bin.

The division of the TPC results in 36 bins per z-slice and therefore 1620 bins in total. In order to create an LCE map, the mean values of S1 are normalised by the average of all S1 data. The relative LCE is then obtained by following equation:

$$LCE(r,\phi,z) = \frac{S1(r,\phi,z)}{\langle S1\rangle} = \frac{\epsilon_L(r,\phi,z)\cdot PY(E,F)}{\langle \epsilon_L \cdot PY(E,F)\rangle} \tag{2.7}$$

With this map a correction to S1 can be applied, accounting for geometrical effects as well as field effects of the detector for the specific incident energy of the observed interaction. For application to the data an interpolation method can be used, which results in a continuous map instead of discrete bins. Therefore it can be applied to each collected S1 signal, leading to a constant S1 for an interaction of a specific energy. The explicit use of an application is not intended to be investigated in this thesis but can be examined in further works. Relative LCE maps can be built with S1 data from ^{83m}Kr decays. Therefore, the properties of ^{83m}Kr as a calibration source in XENONnT are discussed in the next section.

2.4 Calibration with ^{83m}Kr

For the energy calibration in XENONnT sources possessing a mono-energetic decay are used. The detectors response to these is used for calibration, because the recoil energy of an observed interaction can be assigned to the decay energy. For low energetic calibration and position correction, internal calibration sources are used due to the high shielding from outer radiation and the self-shielding abilities of the liquid xenon. External calibration sources can also be used but not explicitly for spatial corrections, because they are not homogeneously distributed in the TPC. The calibration considered in this work makes use of the meta-stable isotope ^{83m}Kr. As shown in figure 2.3, ^{83m}Kr is obtained by an electron capture of ^{83}Rb, followed by two decays. The first decay has a half-life of $T_{1/2} = 1.83\,\text{h}$ and an energy of $\Delta E = 32.2\,\text{keV}$ and the second one a half-life of $T_{1/2} = 154\,\text{ns}$ and an energy of $\Delta E = 9.4\,\text{keV}$. The energies from the decay of ^{83m}Kr are used to calibrate the detector. ^{83m}Kr is brought into the TPC by mixing GXe with gaseous ^{83m}Kr from ^{83}Rb decays outside of the detector. About 90% of this mixture gets liquefied and is added to the LXe in the TPC, while the rest is added to the GXe part at the top of the TPC [17]. ^{83m}Kr is homogeneously distributed in the detector, which is important for spatial corrections and calibrations. The half-life of $T_{1/2} = 1.83\,\text{h}$ is long enough to distribute ^{83m}Kr evenly in the detector and perform a calibration, but also short enough to exclude influences on the background radiation after the calibration is done. Due to the high statistics, the well known energy and the decay scheme, the calibration interactions are well separable from background events.

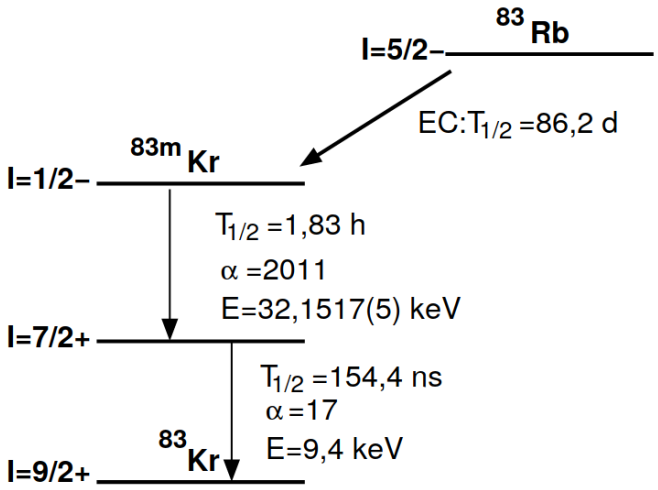

Figure 2.3: Decay scheme of ^{83}Rb and ^{83m}Kr to the stable ^{83}Kr state, taken from [18]. The ^{83m}Kr decay happens in two stages after an electron capture of ^{83}Rb.

In XENONnT the data are processed with the data processing software *straxen* (Streaming Analysis For XENON) [2]. Straxen processes the data, provided by the data acquisition system of XENONnT and classifies them as peaks, which can either be S1, S2 or unknown. The peaks are then identified as a specific event, containing S1 and S2 signals. An event contains the light signals, the time difference between them and the kind of event, in this case krypton decay. In the case of ^{83m}Kr, S1 signals can be separated with respect to their energy. With the decays happening nanoseconds after each other, they can be divided in sections a and b where a denotes the main peak of the signal and b the second largest peak of the signal. $S1_a$ corresponds to the 32.2 keV decay, whereas $S1_b$ describes the 9.4 keV decay. The center time difference between the two signals is denoted as dT. It is not always possible to split the S1 signal in parts a and b because straxen has a limited resolution, which lies in a similar time range with decays of a short lifetime [2]. The merged signals are denoted as single S1. Because it is the sum of the $S1_a$ and $S1_b$ peaks, the energies of the decays add up to 41.6 keV. Therefore, three different S1 signals for ^{83m}Kr decays can be recorded. The main focus in this work lies on the $S1_a$ and $S1_b$ signals instead of the merged S1 signal. If a peak is not classified as S1 by straxen, it has to be an S2 peak or is classified as unknown and removed from the data set. The signal width of S2 is in general higher than the half-life of the krypton decay with a signal width in the µs range [5]. Therefore, it is not possible to split S2 into $S2_a$ and $S2_b$, corresponding to the split S1 signals.

Because it is necessary for photon yield simulations in the next chapter (3) to define the time difference between $S1_a$ and $S1_b$, a mean value of dT is calculated for the data set used of ^{83m}Kr events. A histogram with an exponential decay fit to the time difference of $S1_a$ and $S1_b$ is shown in figure 2.4. For the estimation of a mean dT, a reasonable value from the time

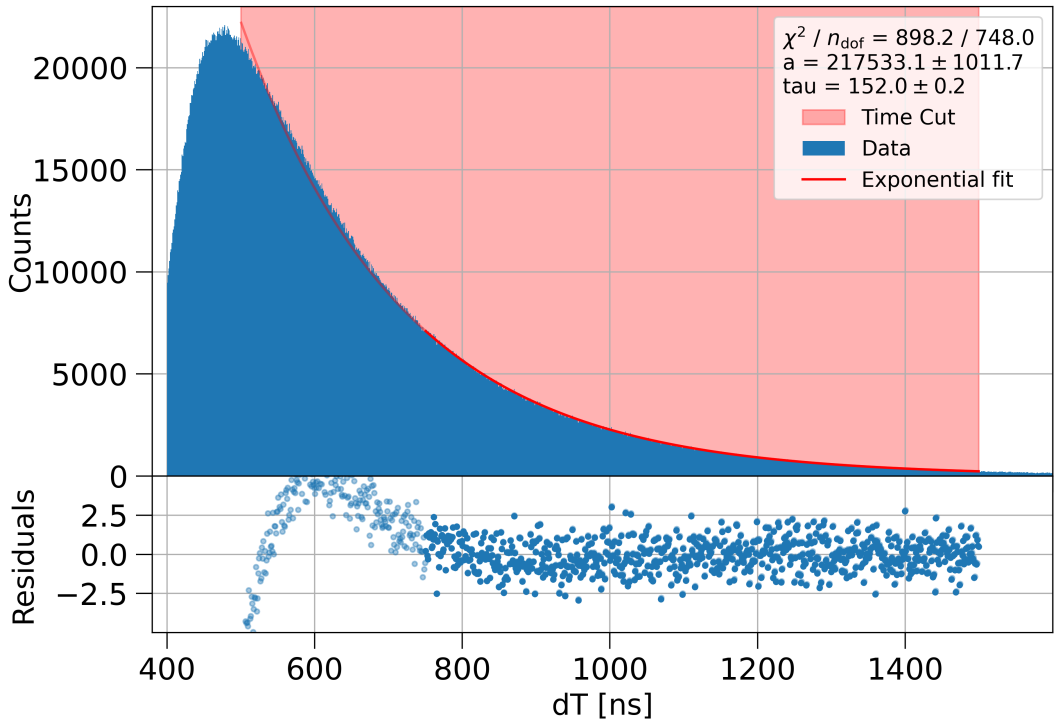

Figure 2.4: Histogram of the time differences dT between $S1_a$ and $S1_b$, with a shaded region, showing the cuts made for dT. The exponential fit is shown in red and the residuals are shown below. For an unrestricted fit range the exponential fit is shown in transparent red and the residuals in transparent blue.

differences in the data has to be found. A first cut at 500 ns is made because events prior to this time have a higher chance not to be separated correctly into $S1_a$ and $S1_b$ than after the maximum value of the dT distribution. The second cut is applied at 1500 ns because there is only a small chance of $2 \cdot 10^{-5}$ % for Krypton decays to occur after this time cut. Therefore, most part of the data after it will be background events or are falsely classified as krypton events. Further cuts were made excluding points, whose radial or height coordinates were outside of the TPC's geometry. The weighted mean time difference in the cutoff region is $\langle dT \rangle = (651.4 \pm 0.5)$ ns, which is used for the simulation of the photon yield for the 9.4 keV line. In addition an exponential decay fit is applied to the cutoff region. This fit should result in the half-life for the second decay with $\tau = 154$ ns and is added to verify the half-life in the data. The exponential fit function thus is

$$f(t, A, \tau) = f(t, \theta) = A \cdot \exp(-t \cdot \log(2)/\tau) \tag{2.8}$$

with an amplitude A and the half-life τ and a fit range from 750 ns to 1500 ns. A restricted fit range is used, because an unrestricted fit range would lead to strong deviations in the

residuals from 0. The unrestricted fit in the full cut range is shown in transparent colors in figure 2.4. For small dT, straxen may not be able to separate all events correctly into $S1_a$ and $S1_b$, which leads to a count rate that is not high enough to match the exponential fit. The expected counts in this time range should be higher than they are, such that they match the exponential fit. Restrictions in the fit range do not lead to a different $\langle dT \rangle$ because the time cuts are not reduced, in order to obtain high enough statistics. For the estimation of the fit parameters, the method of least squares is used as described in [14]. Therefore, the sum of the residuals has to be minimised, which are defined as

$$res_i = \frac{y_i(t_i) - f(t_i|\theta)}{\sigma_{y,i}(t_i)}\,, \tag{2.9}$$

where y_i is the number of counts per bin, $f(t_i|\theta)$ the fit function evaluated at t_i and $\sigma_{y,i}(t_i)$ the uncertainty in y_i. For the assumption of a counting process and a high statistic in each bin, the uncertainty of y_i is equivalent to $\sigma_{y,i}(t_i) = \sqrt{y_i}$ for large numbers of counts $y_i > 10$. For an analysis of the goodness of the fit, the reduced χ^2_{red} is defined as

$$\chi^2_{red} = \frac{\chi^2}{K} \tag{2.10}$$

where K are the degrees of freedom and χ^2 is

$$\chi^2 = \sum_{i=1}^{n} \left(\frac{y_i(t_i) - f(t_i|\theta)}{\sigma_{y,i}(t_i)} \right)^2 . \tag{2.11}$$

In this case K is defined as

$$K = n - p = 748\ , \tag{2.12}$$

where n is the number of bins in the histogram and p the number of fit parameters. For minimisation of the fit parameters θ the python package *iminuit* is used [15]. The fit parameter $\tau = (152.0 \pm 0.2\,\text{ns})$ shows a deviation of 1.6 % from the nominal value. With the estimated mean time difference, the photon yield of the krypton decay will be calculated with NEST, which is examined in chapter 3.

2.5 The electric field simulation

As mentioned in section 2.2, the electric field inside the TPC is set up by the anode, cathode, gate and the field shaping rings. Because of its influence on the recombination electrons and the resulting photon yield, the drift field is important to understand for the XENONnT experiment. Therefore, a simulation of the field can provide a deeper understanding of interactions in the TPC and energy reconstructions. An explicit correction for field inhomogeneities could

lead to an improvement in correction maps of S1 signals. Because the electric field can not be measured directly inside the TPC, the assumed homogeneous field strength of the drift field is calculated by the voltages of the electrodes. The simulation, provided by Francesco Toschi, uses the voltages from SR0: $V_{\text{anode}} = 4.9\,\text{kV}$, $V_{\text{gate}} = 0.3\,\text{kV}$ and $V_{\text{cathode}} = -2.75\,\text{kV}$. The bottom ring of the field shaping rings is connected to the cathode while the top ring has a voltage of $V_{\text{FSR}} = 0.65\,\text{kV}$ [8]. With this setup of voltages the drift field is determined to 23 V/cm and the extraction field to 2.9 kV/cm. The available information about the voltages at the electrodes are used to create an electric field simulation with the physics simulation software COMSOL [1]. For the creation of this field simulation, a rotational symmetric model of the detector is used as a basis to calculate the electric field for discrete points and interpolate it in three dimensions [19]. Due to the assumed symmetry, the electric field simulation is only illustrated in r- and z-directions. For the purpose of this thesis, the assumption is

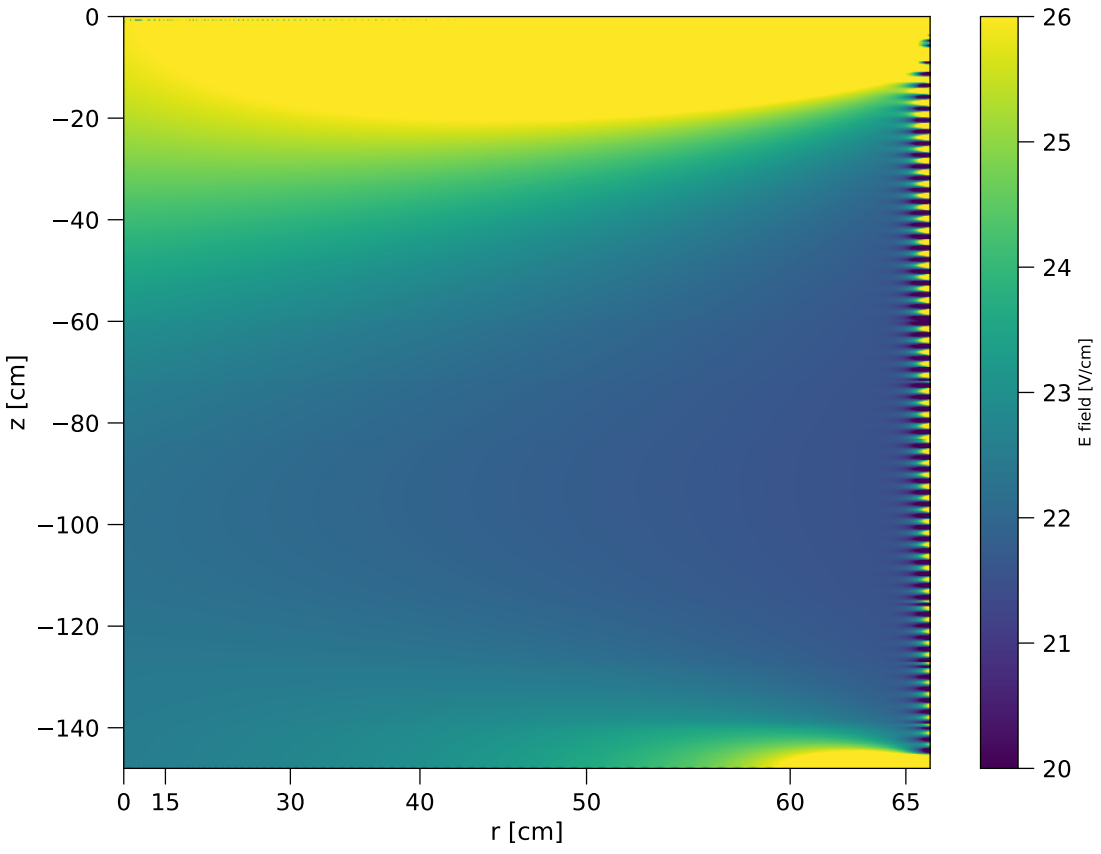

Figure 2.5: The simulated electric field inside the TPC. At the edges of the TPC variations in the field can be observed, corresponding to the shape of the gate, the cathode and field cage. The color bar indicates the electric field in V/cm and is restricted from 20 V/cm to 26 V/cm for better visualisation. At the top and the bottom of the TPC higher voltages occur due to the gate anode and cathode. For high radii the alternating voltages of the field shaping rings can be observed.

justified, although further investigations of angular effects in the TPC could be necessary. The result of the simulation is shown in figure 2.5. It can be observed that the field is nearly homogeneous for an inner volume of $-138\,\mathrm{cm} < z < -40\,\mathrm{cm}$ and $0\,\mathrm{cm} < r < -63\,\mathrm{cm}$ with an electric field strength of $F = 22.65\,\mathrm{V/cm}$. For high z-coordinates $z > -30\,\mathrm{cm}$ the influence of the gate and the anode leads to higher values of the electric field which exceed the limits of the color bar. At high radii the influence of the field shaping electrodes can be observed by an alternating field strength which provides the homogeneity of the electric field. This also exceeds the upper and lower limits of the color bar. On the bottom for high radii another population of high electric field strength can be found, due to the influence of the cathode. The average electric field strength of $F_0 = 23.66\,\mathrm{V/cm}$ in the simulation is close to the nominal value of $23\,\mathrm{V/cm}$ with a deviation of $2.9\,\%$. Because it can not be measured directly inside the TPC, the field simulation is a promising approach for modeling the drift field. By modeling the influences of all electrodes and the field cage, the simulation provides a basis for a field correction to S1 data in combination with NEST.

3 The Noble Element Simulation Technique (NEST)

The Noble Element Simulation Technique is a simulation software to describe scintillation yields in liquid xenon and other noble elements [21]. With its comprehensive approach, NEST can be used in XENONnT to calculate photon yields. This chapter introduces the working principle of NEST and photon yield calculations. Furthermore the effects of the electric field and the time difference between $S1_a$ and $S1_b$ on the simulated photon yield are analysed. With the combination of NEST and the field simulation a field correction for S1 signals can be calculated.

3.1 Introduction to the Noble Element Simulation Technique

NEST is a detector and experiment independent simulation software for excitation, ionisation and scintillation processes in liquid noble elements [21]. It can describe the non-linear energy and field dependence of the scintillation and ionisation yield for electronic recoils and nuclear recoils with its comprehensive and quasi-empirical approach of photon yield simulations. For this purpose, experimental results from noble element experiments are used in different energy and electric field ranges as a data basis [21]. Especially in xenon experiments, NEST is a suitable analysis tool for photon yield simulations. While NEST was originally implemented in Geant4 and C++, this work uses the Python bindings for the NEST library NESTpy. The focus of this thesis is set on electronic recoils from krypton calibration. For electronic recoils, the ionisation and scintillation are considered as channels for an energy deposition. The third channel is energy lost to heat and can not be recorded in XENONnT. A near 100 % efficiency for excited or recombined electrons to lead to S1 is assumed and the kinetic energy of ionization electrons is present in the work function for ionisation W_i [21]. The deposited energy E_dep of a particle from a single interaction is then defined as

$$E_\mathrm{dep} = N_\mathrm{ex} W_\mathrm{ex} + N_\mathrm{i} W_\mathrm{i} = N_\mathrm{i}(\alpha W_\mathrm{ex} + W_\mathrm{i}) \ , \tag{3.1}$$

where N_{ex} is the number of excitons and N_{i} the number of ions per energy deposition. W_{ex} and W_{i} are the work functions for excitation and ionisation. $\alpha = N_{\mathrm{ex}}/N_{\mathrm{i}}$ is the exciton to ion ratio which is not a function of energy but shows differences in NR and ER interactions, as well as a dependence on the electric field [21]. The theoretical value for α is constant for LXe with $\alpha = 0.06$ [23] but some experimental results determine α to 0.20 [13]. In order to derive the number of photons N_{ph} and electrons N_{e}, the recombination probability r must be included. Because of the low α, it is assumed that the main part of S1 originates from recombination processes. This leads to the equations

$$N_{\mathrm{ph}} = N_{\mathrm{ex}} + rN_{\mathrm{i}} \text{ and} \tag{3.2}$$

$$N_{\mathrm{e}} = N_{\mathrm{i}}(1 - r)\,. \tag{3.3}$$

The recombination probability is calculated with two models. For long particle tracks, NEST uses a modified version of Birk's Law as derived from Doke et al. [12]. This model for recombination probability is strongly dependent on the energy loss per unit of path length $\mathrm{d}E/\,\mathrm{d}x$ and is constructed from the cross-section of a long track of electron-ion pairs. As $\mathrm{d}E/\,\mathrm{d}x$ approaches infinity, r approaches 1. The second model used in NEST is the Thomas-Imel box model, which is more accurate for short particle tracks [20]. It describes the electron-ion recombination for low energetic recoil events of short particle tracks in a "box" geometry [24]. Short particle tracks are defined as those that are shorter than the mean ionisation electron-ion thermalisation distance [21]. These shorter tracks can generally be allocated to lower energetic particles. The Thomas-Imel box model is independent of $\mathrm{d}E/\,\mathrm{d}x$ and has a different approach than the Doke/Birk's model. Instead of a long column of electron-ion pairs a small box geometry is used to describe the scintillation yield for low energetic events with short particle tracks. The combination of those models forms one unified model of scintillation yield, which is continuous with respect to energy and consistent with experimental data. In order to link the models together, nearly all available data on electron recoil scintillation yield are used in NEST [21]. The free parameters of the model are determined by an optimisation process with experimental data. Therefore, the two work functions are combined to a mean work function W for production of either excitons or electron-ion pairs [21]. A combined work function can explain experimental results as well, as two distinct work functions. This results in the deposited energy $E_{dep} = W(N_{\mathrm{ex}} + N_{\mathrm{i}})$. The introduced combined work function leaves the total number of quanta unchanged and therefore does not modify the simulated results.

NEST takes the electric field and the energy deposition as input parameters to simulate the light yield and charge yield of an interaction. For a range of electric fields from 1 V/cm to

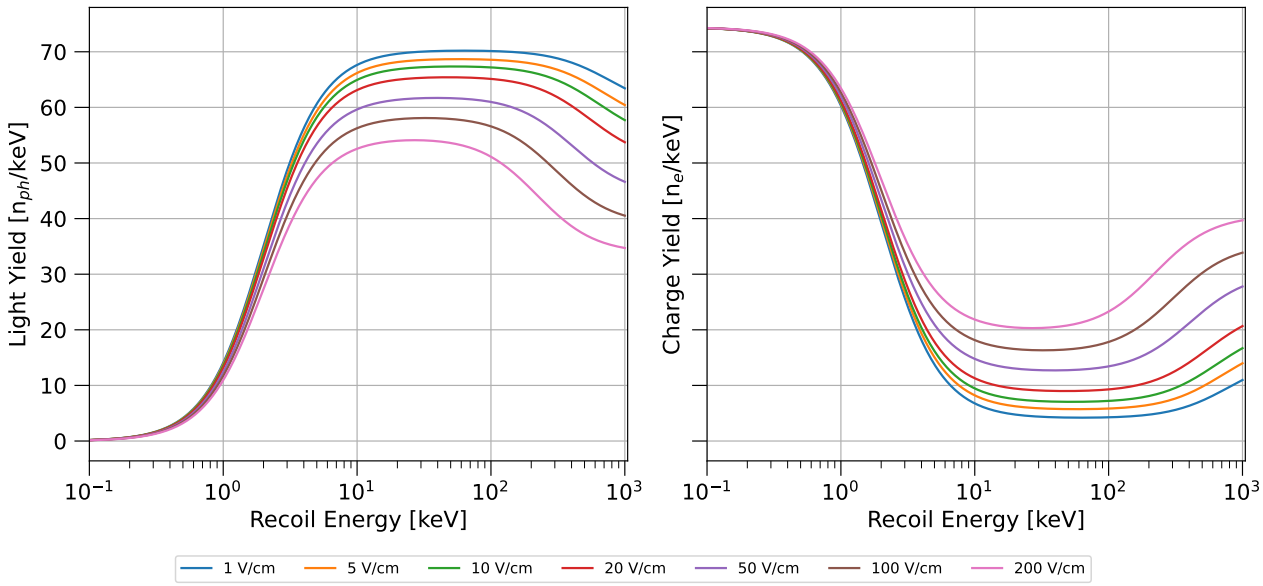

Figure 3.1: The light yield (left panel) and charge yield (right panel) for electronic recoils of the gamma ray interaction type are shown for different electric field strengths ranging from 1 V/cm to 200 V/cm. An anti-correlation between light yield and charge yield can be observed.

200 V/cm and an energy range from 10^{-1} keV to 10^{3} keV the yields are shown in figure 3.1. The interaction type can be brought into the calculations besides the field and the energy. Possible interaction types are neutrons for NR or gamma rays and ^{83m}Kr for ER. The recombination probability and therefore the light yield decreases with increasing energy for Doke model applications. Between 10 keV to 100 keV there is a maximum plateau for each electric field strength caused by the transition to the Thomas-Imel model, which is applied at recoil energies in the energy scale of 1 keV. The light yields and charge yields are anti-correlated as expected from equation 3.3. In general, the yields have constant values for each calculation with NEST. There are no fluctuations in the light and charge yields as long as the values of the interaction type, the electric field and the incident energy are not changed. An exception is the interaction type ^{83m}Kr which is described in section 2.4. For increasing electric field strengths, the light yield decreases and the charge yield increases. This course can be observed in figure 3.1. Since ionization electrons are less likely to enter recombination processes at higher field strengths, the light yield gets smaller. This means a higher field strength leads to an enhancement in S2 and consequently a suppression in S1 [8]. This phenomenon is known as electric field scintillation quenching and approached in NEST semi-empirically, using free parameters from the Thomas-Imel and Doke/Birk's model [21]. In NEST, the yields are always calculated first. After that, the number of photons n_{ph} and the number of electrons n_{e} are calculated, based on the light and charge yields. For the simulation of the number of ions and excitons a fano factor is introduced, which corresponds to a binomial

distribution, leading to fluctuations in the number of excitons and ions [22]. This factor is cancelled out in the light and charge yields of the same incident energy.

Other applications of NEST than yield generation are the modeling of S1 and S2 depending on detector properties. Therefore, detector specific properties like the gains of S1 and S2, g_1 and g_2, have to be taken into account. This work avoids a full detector modeling in NEST. Instead, only the magnitude of the electric field from XENONnT, based on the provided simulation in section 2.5 is used for the simulation of photon yields. With this approach, the influences on yield simulations with NEST are analysed in the following section.

3.2 Influences on the photon yield simulation

As discussed in the previous sections, there are three parameters that can influence the simulated photon yield of the krypton decay. The first parameter is the incident energy. For the interaction type ^{83m}Kr, the energy used for photon yield simulations is either 9.4 keV for PY_a, 32.2 keV for PY_b or 41.6 keV for the merged photon yield. The energy as an input parameter is used by NEST to differentiate between PY_a, PY_b and the merged photon yield. Specifically for the ^{83m}Kr interaction type, the time difference dT between the decays has an influence on the photon yield. The last input parameter for photon yield calculations is the electric field, which influences on the interaction type of gamma rays has been discussed briefly in section 3.1.

Time influence on the photon yield simulation

The half-life of the ^{83m}Kr decay is relevant for photon yield simulations with NEST. First, the time-independent photon yield from the 32.2 keV energy line is calculated and then the photon yield of the 9.4 keV energy line is added. The latter depends on the time difference between the decays dT. If no explicit time difference is passed, a random time from an exponential distribution with the half-life of the decay is taken. The yields of the 41.6 keV energy line are then calculated as the sum of the yields from the separated lines. In order to discuss the influence of dT on the photon yield simulated by NEST, the ratio of PY_b/PY_a is calculated with dT as a variable input parameter. The formation of the ratio is useful as a measure of resemblance between the relative light collection efficiency maps of the different energetic lines from ^{83m}Kr in later chapters. Furthermore, with this method the change in PY_a and PY_b can be analysed simultaneously. The energies for PY_b and PY_a are fixed to the energies of the respective decay and the field strength is fixed for each set of ratios PY_b/PY_a. The result is shown in figure 3.2. Because of the time-independence of PY_a, the ratio PY_b/PY_a is only dependent on the changes in PY_b for different dT, whereas PY_a

has a constant value. It can be observed that PY_b decreases with increasing dT. For lower $dT < 450\,\text{ns}$, PY_b decreases with a higher gradient than for higher dT. This effect can be explained by the circumstance that PY_a is detected only a small amount of time before PY_b. A higher chance of electrons and ions from the track of the 32.1 keV transition that have not recombined, still populating the immediate vicinity of the krypton atom occurs, which leads to a higher recombination probability [4]. Therefore, the slope of PY_b/PY_a decreases for large dT. If the ratio is evaluated over dT at different, constant field strengths, the shape of the curves in figure 3.2 remains the same but a shift towards higher ratios can be observed for increasing field strengths. For example, the mean shift in the ratio from $F = 20\,\text{V/cm}$ to $F = 100\,\text{V/cm}$ is $\Delta\frac{PY_b}{PY_a} = (0.024 \pm 0.001)$. This corresponds to a change in the ratio for the interval from $dT = 240\,\text{ns}$ to $dT = 1200\,\text{ns}$ with $F = 20\,\text{V/cm}$. Thus, an investigation on varying time differences for the photon yield simulations could be necessary for $dT < 400\,\text{ns}$. Due to the cut in the krypton data at 500 ns, this effect should not be prominent in the following analysis.

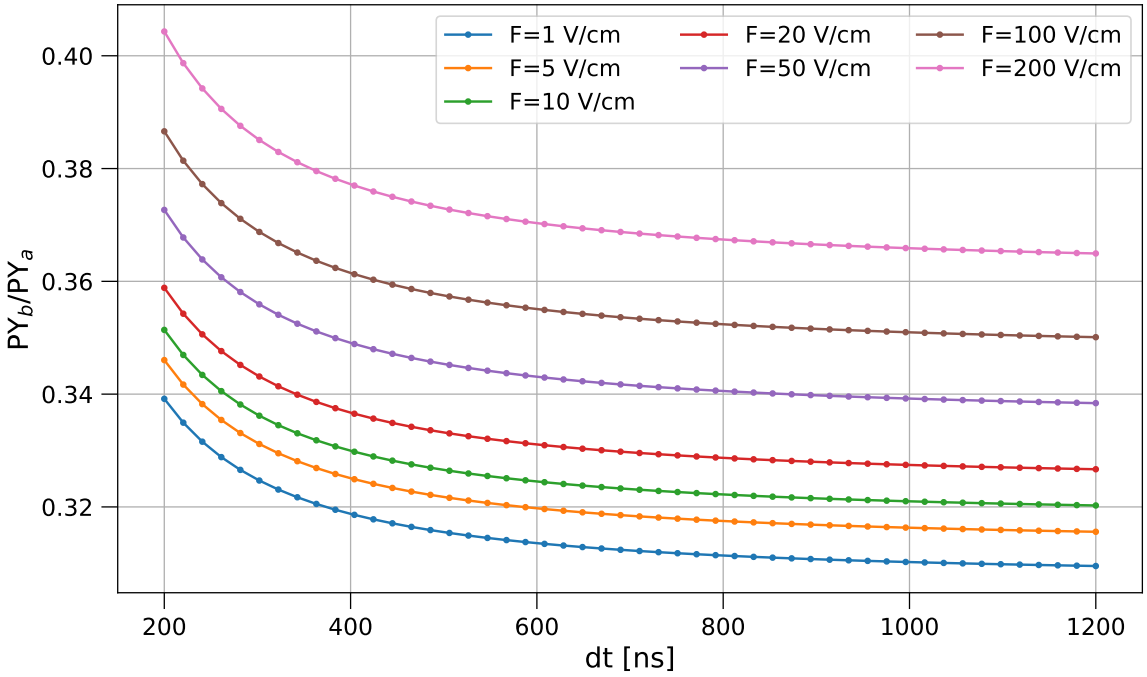

Figure 3.2: The ratio of PY_b/PY_a is simulated for a fixed field strength and variable dT. For each set of calculated ratios a different but constant field strength is used, which is indicated by the different colours. The field strength ranges from 1 V/cm to 200 V/cm.

Field influence on the photon yield simulation

In order to find the electric field strength in the TPC for an observed interaction, the field simulation is used. Thereby, it is possible to convert a position into a field strength with the correctness of the field map as a precondition. The simulated photon yield does not depend explicitly on the position of the interaction in the TPC. Position dependencies arises only via varying electric field strengths at different areas. Due to the assumed radially symmetric detector geometry for the electric field simulation it is only possible to calculate the photon yield in r- and z-directions. In general, it can be assumed that both the light collection efficiency ϵ_L and the electric field F are position dependent. Therefore, only in the case of a constant energy deposition and a constant field strength the averaged value of PY can be separated from ϵ_L as in equation 2.7. For this purpose, the average of all simulated electric field strengths in the TPC is calculated, which leads to a mean field strength of $F_0 = 23.66\,\mathrm{V/cm}$. The time difference between $\mathrm{PY_a}(F)$ and $\mathrm{PY_b}(F)$ is set to $\langle dT \rangle = 651.4\,\mathrm{ns}$, as discussed in section 2.4. For F_0 and the respective energies of the $^{83\mathrm{m}}$Kr decay as input parameters to NEST, the yields $\mathrm{PY_a}(F_0) = 69.2\,N_{\mathrm{ph}}/\mathrm{keV}$ and $\mathrm{PY_b}(F_0) = 61.1\,N_{\mathrm{ph}}/\mathrm{keV}$ are obtained. The simulated photon yield ranges from $55.2\,N_{\mathrm{ph}}/\mathrm{keV}$ to $78.4\,N_{\mathrm{ph}}/\mathrm{keV}$ for $\mathrm{PY_b}$ and from $48.7\,N_{\mathrm{ph}}/\mathrm{keV}$ to $81.3\,N_{\mathrm{ph}}/\mathrm{keV}$ for $\mathrm{PY_a}$ for all positions in the TPC. A visualisation of this effect can be obtained by projecting the photon yield onto each point of the TPC, which is shown for $\mathrm{PY_a}$ in figure 3.3. It can be observed, that the simulated photon yield corresponds to the changes in the electric field strength. Especially for high radii the simulated photon yield is affected by the field cage. At the top and the bottom of the TPC, the influences of the cathode, the gate and the anode can be observed, which leads to decreasing $\mathrm{PY_a}$. In the middle of the TPC, where the electric field is mainly homogeneous, the photon yield is nearly constant with a change of $2\,N_{\mathrm{ph}}/\mathrm{keV}$. The larger effects on the photon yield are visible at the edges of the TPC, resulting from the geometrical distribution of the simulated electric field. With $\mathrm{PY_a}(F_0)$ and $\mathrm{PY_b}(F_0)$, the photon yield can be normalised and a field correction can be calculated.

Furthermore, the ratio $\mathrm{PY_b}/\mathrm{PY_a}$ is used to analyse the influence of the electric field strength on the photon yield simulation. In this case, the field strength is variable and the time difference is fixed for each set of $\mathrm{PY_b}/\mathrm{PY_a}$. The resulting ratios of the photon yield are shown in figure 3.4. With increasing field strengths, the ratio also increases for constant dT. Because a higher-energetic electronic recoil is affected stronger by the electric field than a lower-energetic recoil, a change in $\mathrm{PY_a}$ has more impact on the ratio than a change in $\mathrm{PY_b}$ [21]. Thus, as both photon yields decrease for increasing field strengths, $\mathrm{PY_a}$ decreases more rapidly then $\mathrm{PY_b}$. Over the shown range of the electric field for constant $dT = 650\,\mathrm{ns}$, the change in the ratio is $\Delta\frac{\mathrm{PY_b}}{\mathrm{PY_a}} = (0.018)$. For different but constant dT, a shift towards

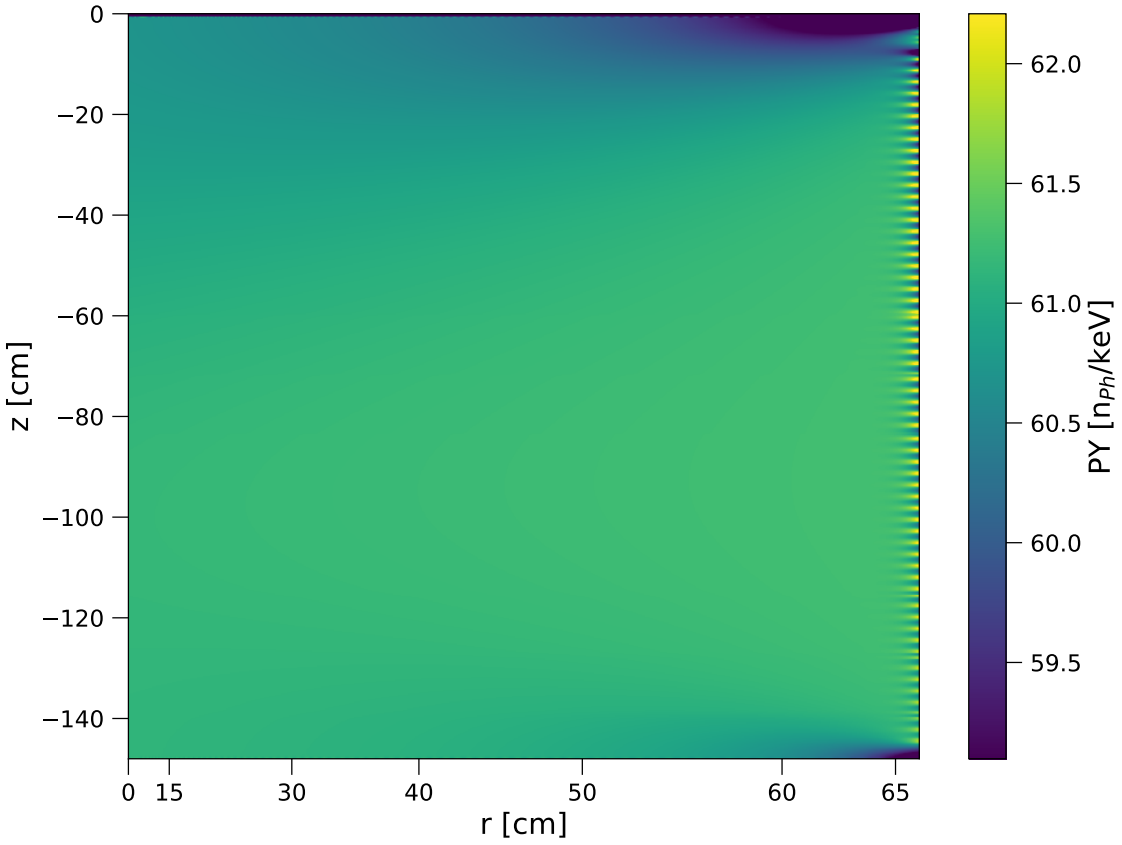

Figure 3.3: The simulated photon yield $\mathrm{PY_a}$ for each point of the electric field. The color bar indicates the photon yield in N_{ph}/keV and is limited for better visualisation. The strength of the photon yield corresponds to the shape of the electric field strength.

higher ratios for higher dT can be observed. The explanation for this shift follows the same argumentation, that is used in the previous section. Due to a higher recombination probability for small time differences between the decays, the ratio $\mathrm{PY_b}/\mathrm{PY_a}$ increases. The mean difference in the ratio between $dT = 500\,\mathrm{ns}$ and $dT = 1000\,\mathrm{ns}$ for the considered range of electric fields in figure 3.4 is $\Delta\frac{\mathrm{PY_b}}{\mathrm{PY_a}} = (0.0059 \pm 0.0002)$. With a decrease of 67 % it is small compared to the previously calculated changes in ratio for varying dT. This indicates larger impacts on the ratio for changes in the field than changes in dT. Therefore, the restriction to a mean value of dT is justified and should not impede the further analysis of the field simulation and NEST.

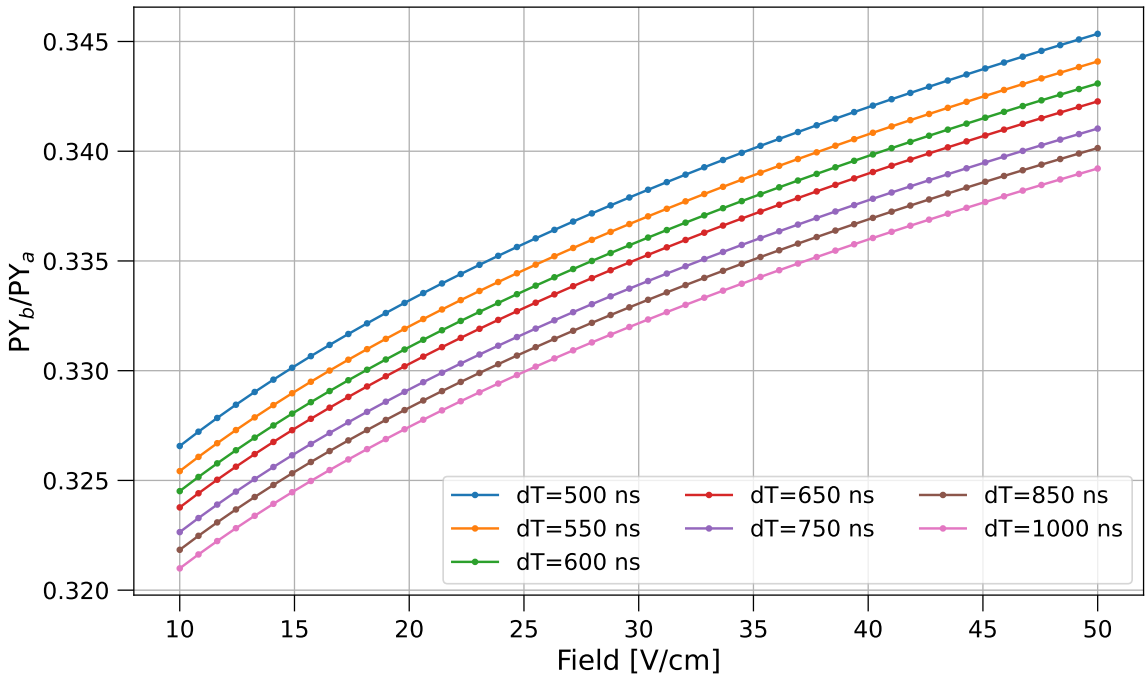

Figure 3.4: The ratio of PY_b/PY_a is simulated for a fixed time difference between the decays and variable electric field strengths. For each set of calculated ratios a different, but constant dT is used, which is indicated by the different colours. The time difference ranges from 500 ns to 1000 ns.

4 Relative light collection efficiency maps

In order to correct S1 for geometric effects, a relative LCE map is formed as explained in section 2.3. For this purpose, the S1 peaks are summarized into spatial bins across the TPC. By analysing the discrete S1 signals in the bins, position and field dependent trends become visible. Two sets of relative correction maps are formed. One contains only information from the recorded data, the other one uses field corrected S1 signals. The applied corrections to S1 are formed by NEST, based on the electric field simulation. This allows a comparison between the supposedly field-free relative LCE maps and the correction maps, that are only based on S1 signals. With this approach, the field corrections N and thus NEST and the field simulation can be assessed in their accuracy.

4.1 Data based relative light collection efficiency

The first set of relative LCE maps does not include an explicit correction for the electric field in its S1 data set. For the properties of the map listed in section 2.3 and the total number of S1 peaks in the used data set, each bin holds approximately 4215 data points for an assumed evenly distributed statistic. In order to determine the mean value of S1 in each bin, a gaussian fit is applied to a histogram of the S1 peaks. The n data points in each histogram are assumed to be independent and identically distributed with a normal probability distribution. Therefore, the distribution of S1 can be determined by

$$f(\mu, \sigma^2, A; x) = f(\theta; x) = A \cdot \frac{1}{\sigma\sqrt{2\pi}} \exp\left(-\frac{1}{2}\left(\frac{x-\mu}{\sigma}\right)^2\right) \tag{4.1}$$

with an amplitude A, the mean μ and the variance σ^2 as fit parameters. The fit parameters, residuals and the goodness of the fit are calculated with the method of least squares as described in section 2.4. The number of bins in each histogram of S1 is chosen with respect to the length of the data set. This ensures comparability for the goodness of the fit in each bin in the LCE maps. Furthermore, each bin in the histogram holds sufficiently high statistics, which allows an estimation for the uncertainty in the number of counts per bin y_i of $\sigma_{y,i}(t_i) = \sqrt{y_i}$. Without an applied field correction, the S1 signals are henceforth denoted as

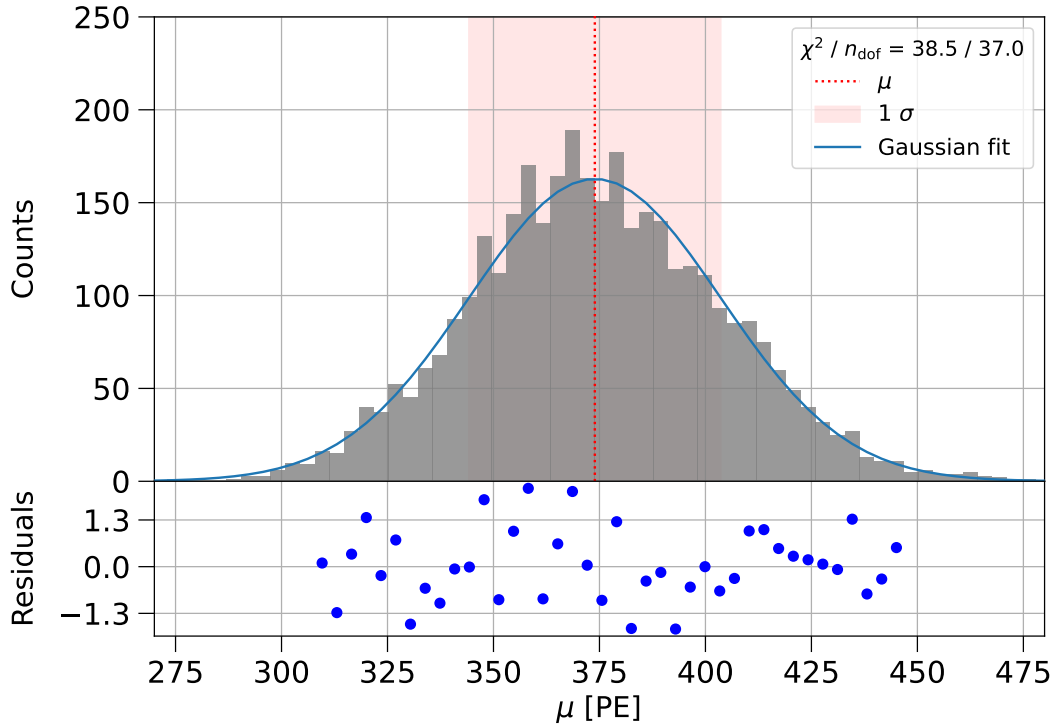

Figure 4.1: Example of a gaussian fit of $S1_a$ for the bin with the centre position $X = (r, z, \phi) = (61\,\text{cm}, -147\,\text{cm}, 3.1)$. The corresponding residuals are shown below. The red line shows μ and the shaded region the 1 σ Interval.

$S1_{a,d}$ and $S1_{b,d}$. For $S1_{a,d}$, the interval of the fit is chosen from 155 PE to 485 PE with 95 bins and for $S1_{b,d}$ from 25 PE to 163 PE with 95 bins. Because of the width of the interval bins occur that can not be perceived as large counts. In order to enable a fit nevertheless, only the regions where the counts fulfill $y_i > 10$ are used for the gaussian fit. With this exception, it is possible for the software *iminuit* to calculate reasonable fit parameters. A disadvantage of this method are the variations in degrees of freedom ranging from 25 to 43. The mean values for the goodness of the fits are $\chi^2_{red} = (1.0 \pm 0.3)$ for $S1_{a,d}$ and $\chi^2_{red} = (0.9 \pm 0.3)$ for $S1_{b,d}$. An example of a bin near the cathode is shown in figure 4.1. The residuals are distributed nearly symmetrical around zero and $\chi^2_{red} = 38.5/37$ is near 1. Therefore, the data can be assumed as normally distributed and fitted with a high value of goodness. In order to create the relative LCE maps, the mean values of $S1_{a,d}$ and $S1_{b,d}$ are normalised by their respective averages $\langle S1_{a,d} \rangle$ and $\langle S1_{b,d} \rangle$ of the whole data set. The relative light collection efficiency calculated from uncorrected S1 signals is denoted as LCE_d and is obtained by equation 2.7. Examples of slices of the relative LCE maps are shown in figure 4.2, where figure 4.2b shows the relative LCE map of the uncorrected $S1_{a,d}$ and figure 4.2a the one of $S1_{b,d}$. An example of a full ranged relative LCE map for $S1_{a,d}$ is shown in the appendix in

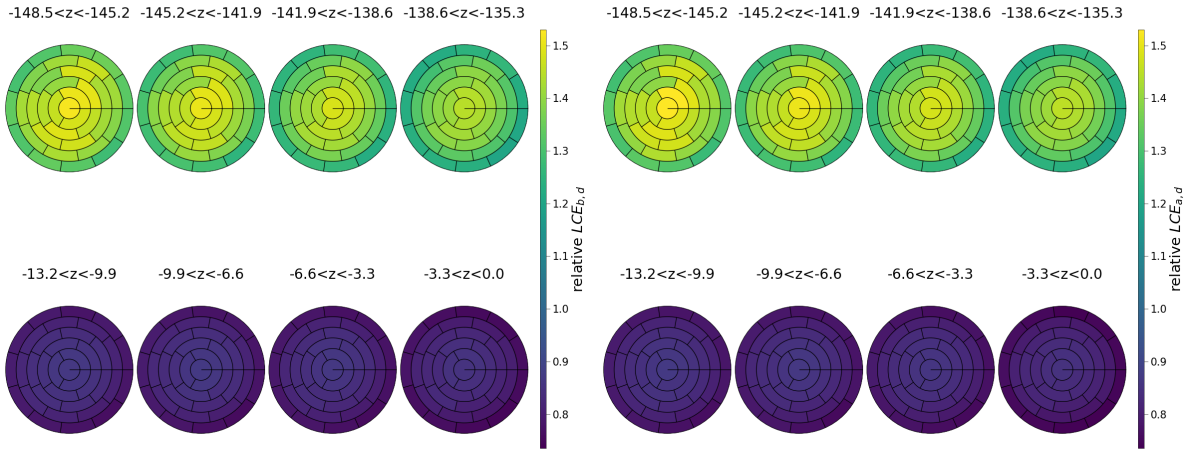

(a) Top and bottom slices of the uncorrected relative LCE map of $S1_{b,d}$.

(b) Top and bottom slices of the uncorrected relative LCE map of $S1_{a,d}$

Figure 4.2: Relative LCE maps of $S1_{a,d}$ and $S1_{b,d}$. These maps are created from uncorrected S1 data. The color bar indicates the relative light collection efficiency and the titles show the coordinates of each z-slice in cm. For increasing z the relative LCE decreases. A similar effect can be seen for increasing radii.

figure A.1. The maps of $S1_{a,d}$ and $S1_{b,d}$ share similar trends and show mainly variations of the relative LCE in height and radial directions. Therefore, the focus of the analysis lies on the z- and r-coordinates rather than the angular coordinates. The strongest dependence of the position can be observed for increasing z, causing a decreasing relative light collection efficiency. In radial direction, the relative LCE also declines for increasing radii. The relative light collection efficiency is higher at the bottom of the TPC then at the top of the TPC as shown in figure 4.2, due to internal reflections at the liquid-gas interface [3]. Furthermore, a strong radial dependency can be observed, lowering the relative LCE for higher radii. This especially is visible in the range of $-148.5\,\text{cm} < z < -128.7\,\text{cm}$. The maximum relative light collection efficiency can be observed at the maximum radius of the bottom z-slice with $\text{LCE}_{\text{a,d,max}} = (1.530 \pm 0.002)$ and $\text{LCE}_{\text{b,d,max}} = (1.518 \pm 0.004)$. For the lowest relative LCE the values $\text{LCE}_{\text{a,d,min}} = (0.735 \pm 0.001)$ and $\text{LCE}_{\text{b,d,min}} = (0.745 \pm 0.002)$ are found at the highest radius of the top z-slice. The uncertainties for the LCE are derived from the gaussian uncertainty propagation. With a comparison of LCE_{d} to correction maps of field corrected S1, the applicability of field-free LCE maps to interactions not limited by a specific energy can be assessed. Furthermore, it can be determined whether they represent an improvement over LCE_{d}.

4.2 Field corrected relative light collection efficiency

In order to investigate the influence of the electric field on S1, a field corrected signal $\mathrm{S1_f}$ is constructed. With this signal another set of relative LCE maps, denoted as $\mathrm{LCE_f}$ is built, which should only show dependencies on $\epsilon_L(r,\phi,z)$ and $\langle\epsilon_L\rangle$ instead of their product with the photon yield as it does in equation 2.7. While the relative LCE maps described in the previous section are only applicable to S1 signals of a specific energy, correction maps that are not dependent on the energy of S1 could be obtained with this approach. Therefore, $\mathrm{LCE_f}$ is supposed to be freed from effects of the electric field in contrast to $\mathrm{LCE_d}$.

Field corrections N for S1 are calculated with NEST for $\mathrm{PY_a}$ and $\mathrm{PY_b}$ with $\langle dT\rangle = 651.4\,\mathrm{ns}$ by the following equation:

$$N(E,F(r,\phi,z)) = \frac{PY(E,F(r,\phi,z))}{PY(E,F_0)} \tag{4.2}$$

The photon yields at constant F_0 are calculated in section 3.2, leading to photon yields of $\mathrm{PY_b}(F_0) = 69.2\,N_{\mathrm{ph}}/\mathrm{keV}$ and $\mathrm{PY_a}(F_0) = 61.1\,N_{\mathrm{ph}}/\mathrm{keV}$. For the calculation of $\mathrm{PY_a}$ and $\mathrm{PY_b}$ the electric field strengths at the centre of each bin in the TPC are used. Therefore, corrections are directly applied to the binned S1. The field corrected signal $\mathrm{S1_f}$ is then formed by dividing S1 by N. Thus, $\mathrm{S1_f}$ is composed of the energy E, ϵ_L, ϵ_{QE}, ϵ_{CE} and the photon yield:

$$\begin{aligned} S1_{\mathrm{f}}(r,\phi,z) &= \frac{S1(r,\phi,z)}{N(E,F(r,\phi,z))} = \frac{S1(r,\phi,z)\cdot PY(E,F_0)}{PY(E,F(r,\phi,z))} \\ &= E\cdot\epsilon_L(r,\phi,z)\cdot\epsilon_{QE}\cdot\epsilon_{CE}\cdot PY(E,F_0) \end{aligned} \tag{4.3}$$

$\mathrm{S1_f}$ should now ideally be freed from effects caused by the electric field. Only the factor $\epsilon_L(r,\phi,z)$ reflects a position dependence in the signal. Corresponding to equation 4.4, the field-free relative LCE maps are formed by dividing $\mathrm{S1_f}(r,\phi,z)$ by the mean value of all volumes $\langle\mathrm{S1_f}\rangle$, which leads to relative LCE maps dependent only on the relative light collection efficiency:

$$\begin{aligned} LCE_{\mathrm{f}}(r,\phi,z) &= \frac{S1_{\mathrm{f}}(r,\phi,z)}{\langle S1_{\mathrm{f}}\rangle} = \frac{\epsilon_L(r,\phi,z)\cdot PY(E,F_0)}{\langle\epsilon_L\cdot PY(E,F_0)\rangle} \\ &= \frac{\epsilon_L(r,\phi,z)\cdot PY(E,F_0)}{\langle\epsilon_L\rangle\cdot\langle PY(E,F_0)\rangle} = \frac{\epsilon_L(r,\phi,z)}{\langle\epsilon_L\rangle} \end{aligned} \tag{4.4}$$

For field corrected relative LCE maps not only the energy, quantum efficiency and collection efficiency cancel out with their respective means, but also the photon yield can be explicitly

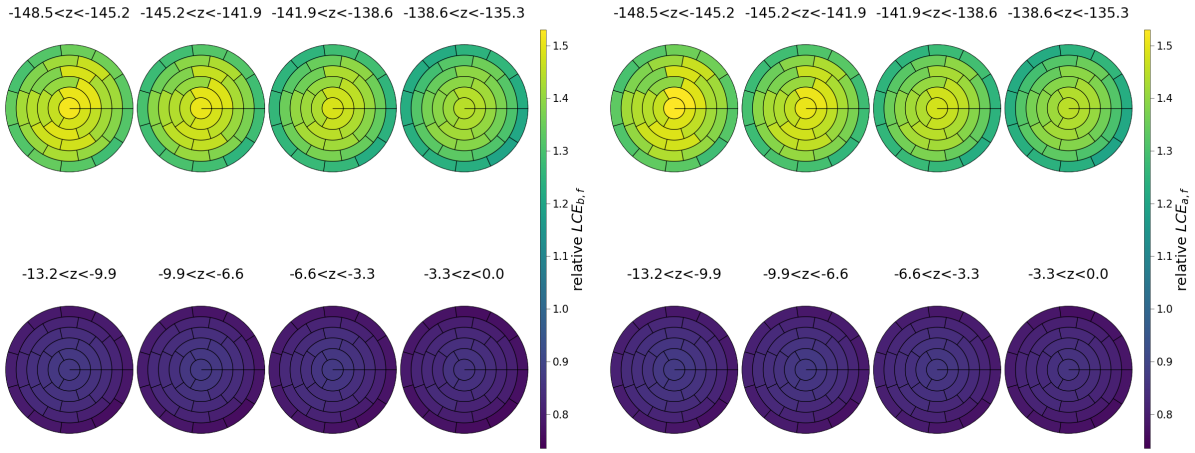

(a) Top and bottom slices of the field corrected relative LCE map of $S1_{b,f}$.

(b) Top and bottom slices of the field corrected relative LCE map of $S1_{a,f}$.

Figure 4.3: Relative LCE maps of $S1_{a,f}$ and $S1_{b,f}$. Here field corrections N are applied to the already binned S1 signals. The color bar indicates the relative light collection efficiency and the titles show the coordinates of each z-slice in cm. The r- and z-dependencies show similar effects as for the relative LCE_d maps.

separated from ϵ_L, because it is a constant, depending only on F_0. The maxima and minima of LCE_f share the same locations as the maxima and minima of LCE_d as described in section 4.1. The maximum light collection efficiencies are $LCE_{a,f,max} = (1.528 \pm 0.002)$ and $LCE_{b,f,max} = (1.517 \pm 0.004)$ and the minima $LCE_{a,f,min} = (0.765 \pm 0.001)$ and $LCE_{b,f,min} = (0.754 \pm 0.002)$. Furthermore, the found trends in radial direction and height are similar to LCE_d. The maps of LCE_f are shown in figure 4.3a and figure 4.3b. All relative LCE maps share the same scale in their color bars, in order to maintain visual comparability. The maximum relative LCE for each energy line decreases by 0.1 % and 0.07 % with an applied field correction for LCE_a and LCE_b, whereas the minimum increases by 3.9 % and 1.2 %. However, this direct comparison between the two maps is just an estimation. A deeper comparison is made in the next chapter by establishing the ratio of the different energy lines as a comparison parameter.

5 Comparison of the relative light collection efficiency maps

As described in section 3.1, variations in the electric field can affect the photon yield of each energy line differently. From this arises the question whether S1 signals of different energetic interactions prepared by field corrections vary weaker than the uncorrected ones in their relative light collection efficiency. This variation is analysed by forming the ratio $\mathrm{LCE_b}/\mathrm{LCE_a}$ from the relative LCE maps determined in the previous chapter. The ratio is described by following equations:

$$\frac{LCE_{\mathrm{b,d}}}{LCE_{\mathrm{a,d}}} = \frac{\epsilon_L(r,\phi,z)\cdot PY(9.4\,\mathrm{keV}, F(r,\phi,z))}{\langle \epsilon_L \cdot PY(9.4\,\mathrm{keV}, F(r,\phi,z))\rangle} \cdot \frac{\langle \epsilon_L \cdot PY(32.2\,\mathrm{keV}, F(r,\phi,z))\rangle}{\epsilon_L(r,\phi,z)\cdot PY(9.4\,\mathrm{keV}, F(r,\phi,z))} \tag{5.1}$$

and

$$\frac{LCE_{\mathrm{b,f}}}{LCE_{\mathrm{a,f}}} = \frac{\epsilon_L(r,\phi,z)\cdot PY(9.4\,\mathrm{keV}, F_0)}{\langle \epsilon_L \cdot PY(9.4\,\mathrm{keV}, F_0)\rangle} \cdot \frac{\langle \epsilon_L \cdot PY(32.2\,\mathrm{keV}, F_0)\rangle}{\epsilon_L(r,\phi,z)\cdot PY(9.4\,\mathrm{keV}, F_0)} \tag{5.2}$$

In equation 5.2, the photon yield cancels out because it is a constant, depending only on F_0 as described in equation 4.4. The result of the ratio is therefore equal to 1:

$$\frac{LCE_{\mathrm{b,f}}}{LCE_{\mathrm{a,f}}} = \frac{\epsilon_L(r,\phi,z)}{\langle \epsilon_L\rangle} \cdot \frac{\langle \epsilon_L\rangle}{\epsilon_L(r,\phi,z)} = 1 \tag{5.3}$$

However, since the electric field is not completely homogeneous as indicated by the field simulation, deviations from 1 can be found in the uncorrected data set. The ratio $\mathrm{LCE_{b,f}}/\mathrm{LCE_{a,f}}$ is not equal to 1 for all considered data points as well, because the used simulations are likely not to be perfectly accurate for all effects in the TPC. Since it is not possible to estimate uncertainties in NEST and the field simulation, the combination of these is assumed to be causing deviations from the expected value. The ratio is formed for comparison whether the field corrected relative LCE maps have a higher resemblance for the different energy lines of $^{83\mathrm{m}}$Kr than the uncorrected ones and to evaluate in which cases it is advantageous to use $\mathrm{LCE_f}$ instead of $\mathrm{LCE_d}$.

Due to the assumed radially symmetrical geometry of the detector and the negligible angular dependencies, the relative LCE is analysed in its z- and r- coordinates. For the summary

of the angular dependent values, the mean values between the adjacent radii, called rings, in each z-slice are calculated. In addition to the error propagation, the calculation of the mean value also contributes to the uncertainty of the ratio. Through the summarised values, an evaluation of the relative LCE ratios in z-direction per corresponding ring is possible and trends become visible. A distinction is made between five cases, that can occur in the comparison and two variables are introduced, which describe the differences of the ratio to 1. These are used as a measure to describe the effects of the electric field. The difference to 1 between $\mathrm{LCE_d}$ is henceforth referred to as α, with

$$\alpha = 1 - \frac{LCE_{\mathrm{b,d}}}{LCE_{\mathrm{a,d}}} \tag{5.4}$$

and the difference to 1 between $\mathrm{LCE_f}$ as β, with

$$\beta = 1 - \frac{LCE_{\mathrm{b,f}}}{LCE_{\mathrm{a,f}}}\,. \tag{5.5}$$

For an ideal, constant drift field and a perfect photon yield simulation with NEST, α and β would be equal to 0. If applications of N to S1 would lead to $\beta = 0$ for cases where $\alpha \neq 0$, NEST and the electric field simulation in combination are supposed to perform a "perfect" correction and therefore provide a field-free relative LCE map. Since this is not always the case, a case distinction is necessary. It is estimated that the effect on β is more likely to be induced by $\mathrm{LCE_a}$ than by $\mathrm{LCE_b}$ because the signal of the 32 keV energy line is more susceptible to changes in the electric field. It decreases with a higher slope for increasing field strengths compared to the 9 keV line, because of its proportionality to the photon yield. This estimation is mentioned in section 3.2, where the influence of the electric field on the ratio $\mathrm{PY_b/PY_a}$ is analysed. Therefore, the differences in α and β are most likely to occur for cases of strong, sudden field changes. If $\alpha < 0$, the ratio of the relative LCEs becomes larger than 1 and the differences in the energy lines increases. This in turn suggests, that an increasing field strength is not accounted for in the ratio of the relative LCE maps. In the opposite case of $\alpha > 0$, the ratio gets smaller than 1. This is most likely caused by an unexpected decrease of the field strength, which is not represented in the relative LCE maps. Since β is based on the field corrected data, an increasement towards 0 as opposed to α is expected. In order to assess the variation among the mono-energetic relative LCE maps for β, it is compared to α. For a graphical comparison between the cases, different colours are used with following distinctions:

- $|\alpha| > |\beta|$: This case covers an approach of $|\beta|$ towards 0 as opposed to $|\alpha|$. Therefore, the influence of the electric field is corrected by N and is mainly cancelled out in the relative LCE maps. Resemblances between $\mathrm{LCE_{a,f}}$ and $\mathrm{LCE_{b,f}}$ increase which is rated

as an improvement compared to $\mathrm{LCE_d}$. The stronger the field correction, the smaller is $|\beta|$ in contrast to $|\alpha|$. This case is shown in green in the plots below. Bins that belong in this category are referred to as "green" bins. If $|\beta|$ was equal to 0 for all areas in the TPC, a "perfect" correction map would be found, that accounts for all electric field effects.

- $\beta > \alpha > 0$ or $\beta < \alpha < 0$: In this case, the explicit inclusion of N in the relative LCE maps does not result in a correction towards 0 but in further deviations between the relative LCE maps of different energy lines. The effect of the field corrected maps draws in the wrong direction away from 0, which means that $|\beta| > |\alpha|$ but the sign of α and β is the same. If α and β still agree in their interval of confidence for their respective uncertainties, this case is indicated by a blue colour. Otherwise, it is shown in violet.

- $\alpha > 0 > \beta$ or $\alpha < 0 < \beta$: As in the previous case $|\beta| > |\alpha|$, but here different signs of α and β indicate a correction attempt in the right direction. If $\alpha < 0$, N should lead to an increasement in β compared to α and if $\alpha > 0$, β should decrease compared to α. In this case an overcorrection scenario arises. If α and β still agree in the interval of confidence for their respective uncertainties, the color yellow is used for visualisation, otherwise the color orange is used.

For each ring, α and β are shown as a function of z. The rings are indexed from the inner to the outermost ring from 1 to 6 and the colours of the bins represent the different cases that can occur. The results of the inner ring and the two outer rings are shown in figure 5.1, 5.2 and 5.3, the other ones in the appendix in figure A.2, A.3 and A.4. In order to evaluate the results in each ring, the number of bins for each possible scenario, the maximum deviation of β from α and the mean deviation is tracked in table A.1. The number of bins for each case indicates how often N leads to an approach or a deviation towards 0 for β compared to α. The maximum deviation describes the maximal effect and the mean deviation the mean effect of N on the ratio. In total, 69.3 % "green" bins, 11.9 % "yellow", 3.0 % "orange", 16.3 % "blue" and 1.1 % "violet" bins occur. In terms of total quantity, the "green" bins are dominant. These indicate an LCE map of higher accuracy in contrast to $\mathrm{LCE_d}$. Therefore, $\mathrm{LCE_f}$ is rated as applicable for signal corrections without restrictions to a specific interaction energy. In this context, applicability means that the conditions set up above for the "green" cases are fulfilled. The next kind of bins with 32 and 44 counts are the "yellow" and "blue" bins, describing cases in agreement for their respective uncertainty range. These together account for 28.2% of all entries. The cases where α and β do not agree in their uncertainty ranges take up 4.1% of the total number of bins. This suggests that the majority of the results produced by $\mathrm{LCE_f}$ fulfill the criteria for an applicable field-free correction map and are seen as an improvement to $\mathrm{LCE_d}$. Nevertheless, a high proportion of the results show that the

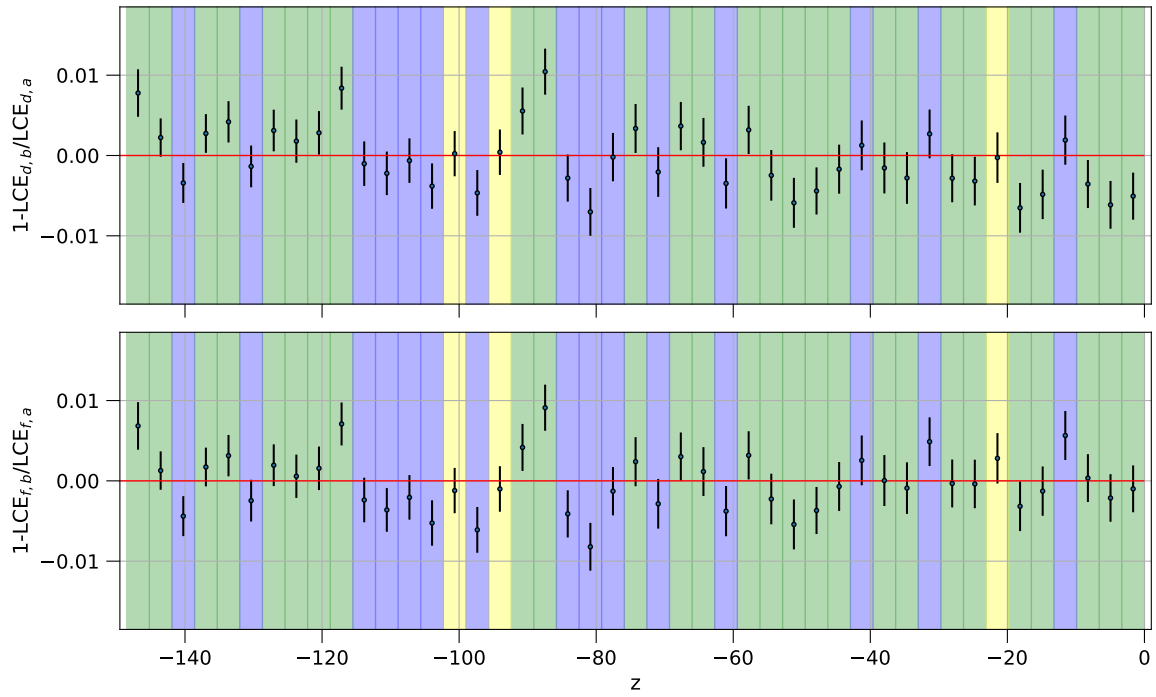

Figure 5.1: For the ring between 0.0 cm and 11.1 cm, α and β are plotted against z. The colors of the shaded regions are explained in the text (page 30). The uncertainties and variations are larger than in the other rings. These, and the high number of "blue" bins are the most striking feature of the inner ring.

map is not freed from field effects at all areas in the TPC. These spatial dependencies are analysed in the following and projected back onto the electric field.

With the coordinates of each data point and its corresponding field strength a projection back onto the electric field simulation can be visualised. The result of the projection is shown in figure 5.4. The figure shows the electric field simulation in z- and r- coordinates with differently coloured bars plotted above, which represent the cases that can occur. These are oriented to the intervals of the individual rings and heights of the z-slices. The results are limited to the uncertainties of the relative LCE maps and the field simulation. Since NEST does not report uncertainties, the photon yield calculations with NEST in combination with the field simulation can be a reason for $\beta \neq 0$. Since 187 of 270 "green" bins are observed, a general improvement of the relative LCE maps in excluding field effects can be assumed. Nevertheless, certain spatial trends are noticeable, where N does lead to an overcorrected ratio or no correction at all.

At the inner ring with radius 0.0 cm $< r <$ 11.1 cm, 27 "green" bins and 15 "blue" bins occur (figure 5.1). Because of the high number of "blue" bins β can not be ascertained as freed from field effects. Nevertheless, all values of α and β in the inner ring of the TPC agree within their ranges of uncertainty. The electric field is mostly homogeneous as indicated by

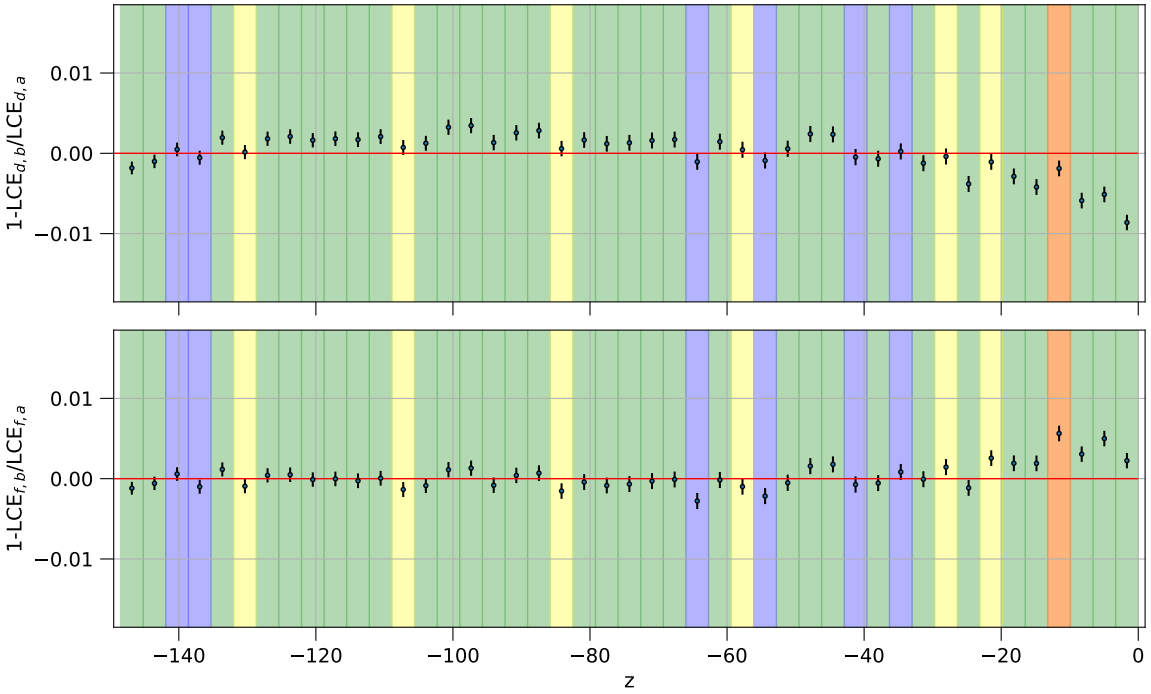

Figure 5.2: For the ring between 44.3 cm and 55.4 cm, α and β are plotted against z. The colors of the shaded regions are explained in the text (page 30). A trend in stronger corrections N towards high z can be observed.

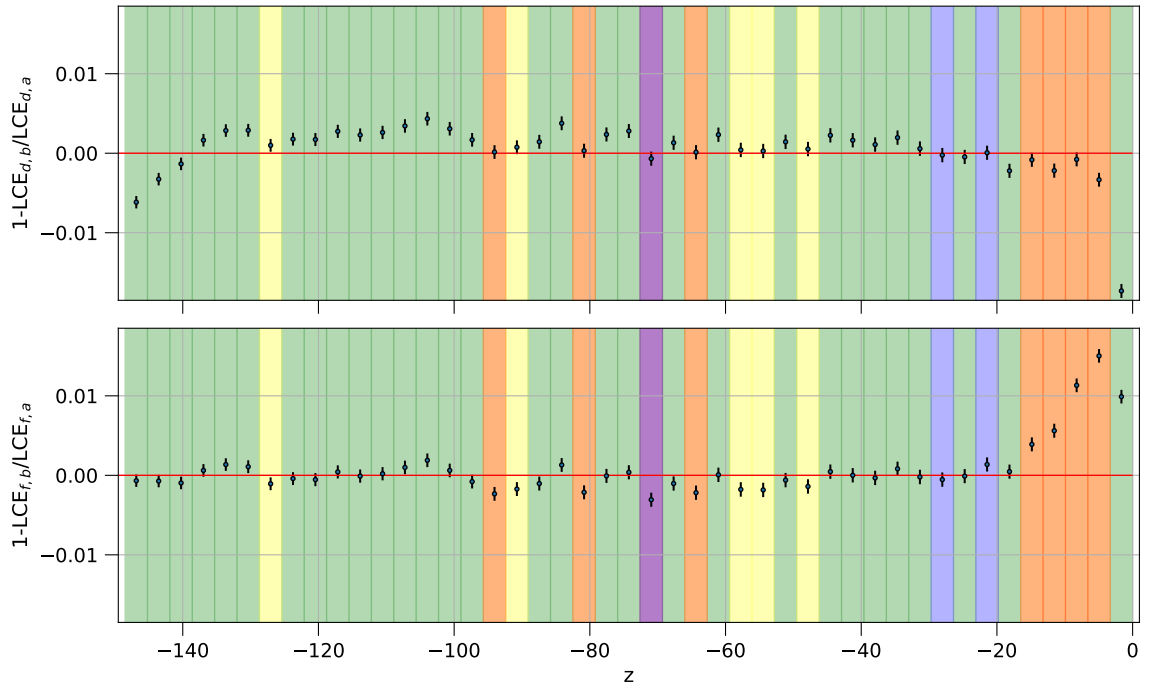

Figure 5.3: For the ring between 55.4 cm and 66.5 cm, α and β are plotted against z. The colors of the shaded regions are explained in the text (page 30). In general, the effect of N is larger than in the other cases. With increasing z, an increasing number of overcorrected bins can be observed.

the field simulation, showing a change of 0.27 V/cm in the considered interval. Despite this circumstance, "green" bins only make out 60 % of all bins in this ring. The positions of "blue" bins tend to be at z from -77 cm to -118 cm. Although the used method fails to produce a relative LCE map only dependent on ϵ_L in these areas of the TPC, this effect can be explained by the large values of uncertainties and does not necessarily correspond to strong changes in the electric field. Due to the binning of the preceding relative LCE maps, less statistics in this ring lead to higher uncertainties than in the other rings. This explains the amount of 15 "blue" and 27 "green" bins instead of a larger number of "green" bins, which would be expected from a homogeneous electric field. Furthermore, the positions of the "blue" bins do not seem to follow a structure specified by the field. Instead, the distribution of the bins seems to be more fluctuating than in the other rings. Therefore, a field correction could be covered by the large uncertainties and $\mathrm{LCE_f}$ can not be considered as an improvement to $\mathrm{LCE_d}$ for certain in this area of the TPC.

On the bottom of the TPC for increasing radii, a curve of "blue" and "yellow" bins corresponding to the shape of the electric field edges can be observed. The observed interval ranges from 22.2 cm to 55.4 cm in radial direction and from -148.5 cm to -135.3 cm in height. The changes in the electric field simulation in this interval are 2.23 V/cm. Therefore, transitions to higher field strengths could lead to increasing differences between the different energetic relative LCE maps. Although this effect can be observed in figure A.3, A.4 and 5.2 it decreases for the ring with radii $r > 55$ cm in figure 5.3. Here, only "green" bins occur for $z > -141.2$ cm and therefore the strength of the electric field is considered to be modelled more accurately for this radial interval. Compared to the previous ring in figure 5.2 a larger effect of N and decreasing uncertainties can be observed. The relative LCE maps causing the structured distribution of "blue" bins are not freed from field effects in this case, because the homogeneity of the field could be overestimated in the simulation. A higher change in the electric field could be expected and therefore β is drawn in the wrong direction, away from 0. On the bottom of the TPC the drift field is influenced mainly by the cathode, whose effects could be underestimated, leading to a higher variation in the different energetic maps. Following this consideration, either the electric field near the cathode or the photon yields from NEST are not simulated precisely enough to match the field inside the TPC. Here, $\mathrm{LCE_d}$ could be preferred for corrections in comparison to $\mathrm{LCE_f}$.

Another structure that can be observed is the overcorrection of S1 for high $z > -20$ cm and high $r > 55$ cm with 4 "orange" bins. This trend is shown in figure 5.4 at the top right corner of the TPC and in figure 5.3. According to the simulation, the change in the electric field for $-20\,\mathrm{cm} < z < -1\,\mathrm{cm}$ and $55\,\mathrm{cm} < r < 65\,\mathrm{cm}$ is 82.43 V/cm. The differences between the energy lines in the relative LCE maps occur mainly due to overcorrections for high z and

high radii. For this area in the TPC the maps are not freed from field influences, instead the difference between $|\beta|$ and $|\alpha|$ increases, leading to correction maps that are not applicable in this area and therefore not an improvement to $\mathrm{LCE_d}$. Corresponding to the influence of the field on the ratio, the expected electric field by the field simulation overestimates the field strength, whereas $|\alpha|$ is closer to 0 than $|\beta|$. Nevertheless, this effect could also stem from the photon yield simulation of NEST. In order to achieve values of $|\beta|$ that are closer to 0, the application of N to S1 has to result in smaller effects on the maps. If the field simulation is assumed to be the most influential factor for an overcorrection, the field should be more homogeneous than expected by the simulation in these areas. A possible factor that could lead to a higher uniformity in $\mathrm{LCE_{a,f}}$ and $\mathrm{LCE_{b,f}}$ is the influence of the field from the gate, the anode and the field shaping rings. If the increase in the electric field was to start at higher z than expected by the simulation, the similarities in the relative LCE maps would increase. A tuning of field corrections N for specific areas in the TPC could therefore achieve a higher resemblance in $\mathrm{LCE_f}$ of different energy lines. Although this approach could lead to a smaller field dependency in the correction map, possible inaccuracies of NEST would still be present.

The evaluation of α and β shows that an included field correction in S1 does result in a field-free relative LCE map but is limited to specific area in the TPC. As explained in the cases analysed in more detail, structures can be recognised corresponding to changes in the electric field map. Nevertheless, $\mathrm{LCE_f}$ shows improvements in the resemblance of the different energetic $^{83\mathrm{m}}$Kr lines and therefore presents an improved correction method to $\mathrm{LCE_d}$ for an inner volume of the TPC. In addition, $\mathrm{LCE_f}$ offers the possibility of an application to interactions of different energies in contrast to $\mathrm{LCE_d}$. A tuning of N for specific structures of the electric field could contribute to a stronger resemblance between the energy lines. Furthermore, the assumed geometry of the detector could be a reason for differences between the energy lines. With the exclusion of angular dependencies in the electric field, possible angular field structures can not be taken into account. This problem could be solved by further simulations of the electric field. Another effect on the ratios could stem from the photon yield calculation of NEST for specific changes in the electric field, whose quality has to be further investigated.

The above analysis can be used to examine the quality of the correction maps inside a fiducial volume. A fiducial volume is used for discrimination of background events in the TPC. It is optimised for the most sensitivity while keeping the analysis robust. In XENONnT the fiducial volume for low-energetic electronic recoils can be approximated with a pentagonal shape. It includes 4.15 tonnes of liquid xenon and possesses the coordinates in radial direction and height summarised in table 5.1. With the application of a fiducial volume, areas in the

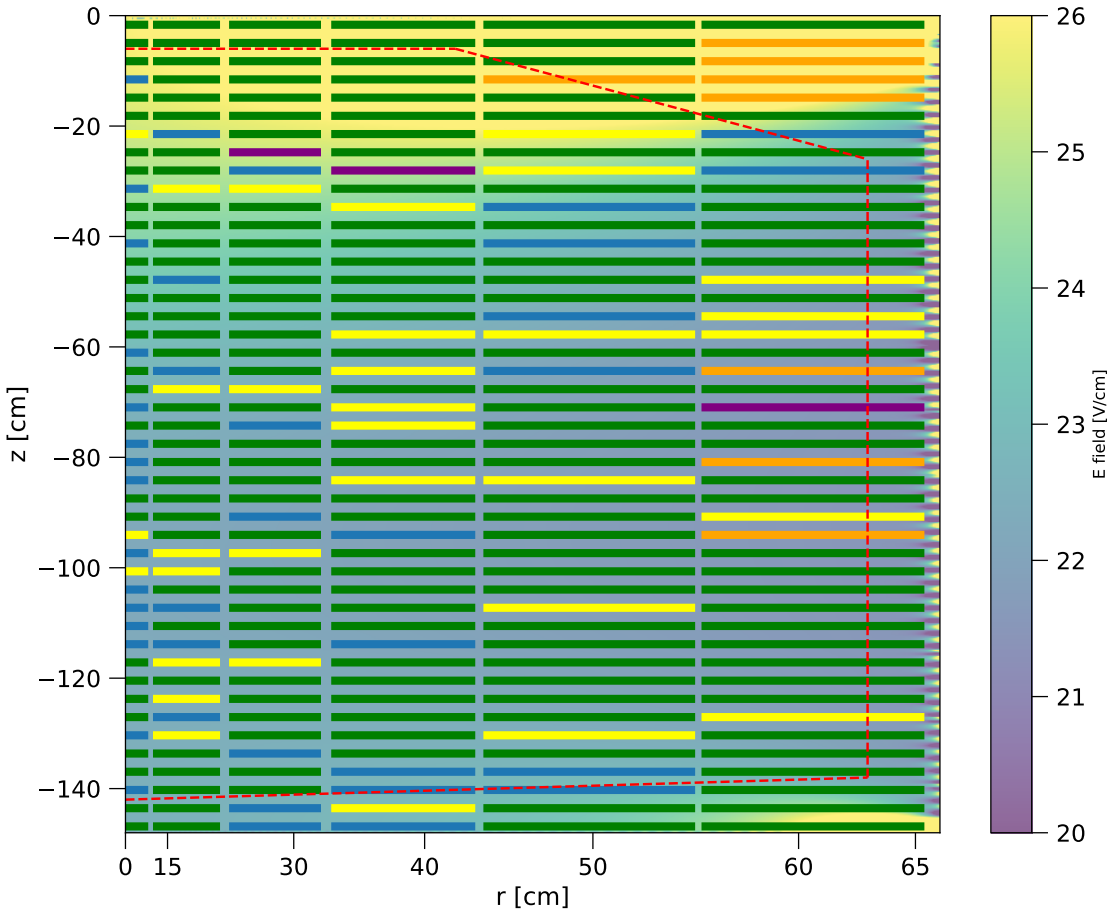

Figure 5.4: The differently coloured bars represent the different cases that can occur in a bin, depending on the r- and z- coordinates in the TPC (page 30). Below, the underlying electric field simulation is shown. The color bar indicates the electric field strength and is limited for better visualisation. Furthermore, the fiducial volume used in XENONnT is represented by the red dashed lines.

TPC containing drastic field changes can be excluded. This is shown in figure 5.4, where the fiducial volume is visualised by the red dashed lines on top of the electric field simulation and the coloured bars, representing the different cases. The restriction to areas inside a fiducial volume should therefore result in further improvements of LCE_f over LCE_d.

Inside the fiducial volume 71.0 % of "green" bins, 24.2 % "blue", 13.4 % "yellow", 1.5 % "orange" and 1.6 % of "violet" bins occur. Since half of the "blue" bins in the fiducial volume are caused by high uncertainties in the centre of the TPC, an application of LCE_f can be justified inside the volumes range. With a contribution of 3.1 %, cases occur where α and β are not compatible within their uncertainty ranges. Especially the exclusion of "orange" bins in the upper right corner of the TPC succeeds by applying the fiducial volume. The majority of "blue" bins at the bottom of the TPC is also excluded. Following these arguments, as well as the application possibilities to different energetic interactions, an improvement of LCE_f over LCE_d in the fiducial volume is established. Consequently, it can be stated that the effects of the electric field within the fiducial volume in LCE_f can be reduced but not completely eliminated.

Table 5.1: The edges for r- and z-coordinates of the fiducial volume used in XENONnT. The radial values range from 0 cm to 63 cm and the height from -142 cm to -138 cm.

r [cm]	z [cm]
0.00	-6.00
42.75	-6.00
63.00	-26.00
63.00	-138.00
0	-142.00

6 Conclusion and outlook

In this bachelor's thesis the effect of the electric field on S1 signals in the time projection chamber of XENONnT has been investigated. For this purpose, the Noble Element Simulation Technique was used to calculate field corrections in the S1 signal and build correction maps. A motivation for this bachelor's thesis was to obtain spatial correction maps that are freed from field effects. Such relative LCE maps would not be dependent on the specific energy of S1 signals. It is also examined whether the field-free correction maps offer an improvement over correction maps that use an uncorrected S1 signal. With this approach the combination of NEST and the electric field simulation and therefore the applicability of the correction maps in XENONnT was analysed. The analysis of the different correction maps draws the conclusion that it is possible to form field-free relative LCE maps and confirms the validity of their application on S1 signal correction. However, these correction maps are limited to specific areas in the TPC. With the simulation of the electric field, spatial trends in the relative LCE maps could be identified and used as an explanation for deviations between the correction maps of different energetic interactions. Furthermore, the supposedly field-free correction maps show improvements over relative LCE maps without a field correction in S1 inside the fiducial volume of XENONnT.

First, ^{83m}Kr calibration data were analysed. Cuts at $dT = 500\,\text{ns}$ and $dT = 1500\,\text{ns}$ were made, which lead to the exclusion of incorrectly assigned events or background events. A half-life fit was applied and the mean time difference between S1_a and S1_b at $\langle dT \rangle = 651.4\,\text{ns}$ was determined, which is used to calculate the photon yield of the 9.4 keV line. Furthermore, the approach for the specific binning of the LCE maps was outlined..

In the second chapter, the photon yield of the NEST simulation was examined. The electric field strength for photon yield simulations is provided by a COMSOL simulation of the electric field inside the TPC of XENONnT. The influences of the electric field on the photon yield simulation were analysed, resulting in a photon yield which corresponds to the distribution of the electric field. It was noticed that PY_a is affected stronger by changes in the electric field than PY_b. Furthermore, the assumption of a constant mean time difference between S1_a and S1_b was justified by analysing the change rates of the ratio $\text{PY}_\text{b}/\text{PY}_\text{a}$ for varying dT and comparing it to change rates for varying field strengths. With a mean photon yield for both

^{83m}Kr energy lines, a field correction N was calculated in the third chapter of this thesis. For each bin in the correction maps a gaussian fit was performed, resulting in a mean value of S1 for each bin. The binned S1 signals were then corrected with N, leading to LCE maps which should be applicable for S1 signal correction without limitations to a specific energy for a homogeneous electric field and an accurate photon yield simulation by NEST.

A comparison between the field-corrected LCE maps and the uncorrected ones is made possible by the ratio of the two mono-energetic lines of ^{83m}Kr. Since the variation between these lines should be minimal for a field-free light collection efficiency map, the differences of the ratio to 1 are used as a comparison medium. Five different cases were distinguished when comparing $\mathrm{LCE_f}$ maps with $\mathrm{LCE_d}$ maps. An improvement in the resemblance between $\mathrm{LCE_a}$ and $\mathrm{LCE_b}$ is reached in 69.3 % of the total events. For those areas, the light collection efficiency is assumed to contain less spatial effects stemming from field influences and is therefore applicable as a correction map to S1 and rated as an improvement to $\mathrm{LCE_d}$. At certain areas inside the TPC, structures could be observed that could stem from an overestimated or underestimated homogeneity of the electric field simulation. Another explanation for these structures are the photon yield simulations with NEST for which no explicit accuracy or uncertainty is reported. At the centre of the TPC high uncertainties arise due to the binning in the LCE maps. In the innermost ring of the TPC 40 % of the bins are not classified as corrected ("green"), which is explained by the uncertainties that could cover the effect of N. Another structure can be observed at $22.2\,\mathrm{cm} < r < 55.4\,\mathrm{cm}$ and $-148.5\,\mathrm{cm} < z < -135.3\,\mathrm{cm}$, where the radial distribution of the electric field simulation causes a decreasing resemblance in the LCE maps between the energy lines. It is not likely that uncertainties from binning statistics have an effect on the correction maps as in the previous case. An influence of the field in this area is the cathode of which the effect could be underestimated by the simulation. Another striking trend can be found for $z > -20\,\mathrm{cm}$ and $r > 55\,\mathrm{cm}$, where overcorrected events occur. In this case a possible explanation is the influence of the electric field from the gate, the anode and the field shaping rings. For the last two cases a tuning of field corrections N could lead to a higher uniformity between the LCE maps. Nevertheless, this would not account for possible inaccuracies of NEST. In addition, the possible cases that can occur for α and β were analysed inside the fiducial volume of XENONnT for low-energetic electronic recoils. The volume excludes overcorrected bins, where α and β do not agree in the interval of confidence for their respective uncertainties and holds 71.0 % of bins, representing the case $|\beta| < |\alpha|$. An application of $\mathrm{LCE_f}$ inside the fiducial volume is therefore justified and perceived as an improvement to $\mathrm{LCE_d}$.

In further works, the application of the results to S1 data of different energies can be tested. In order to improve the resemblance in different energetic field corrected LCE maps, N

could be tuned for areas in the TPC that show structures of unexpected high or low ratios. Furthermore, as the simulation of the electric field does not include angular dependencies, an inclusion could possibly lead to an observation of more detailed spatial trends in the ratios. Further works could also include the merged S1 signal for more statistics and a more detailed analysis. Another influential factor on the creation of field-free correction maps is the choice of $\langle dT \rangle$, where variations and therefore its effects on the LCE maps could be investigated in more detail.

A Appendix

Table A.1: The table shows the number of bins, the maximum deviation and the mean deviation from α to β for each ring R starting to count from the inner ring to the outermost one. The conditions for the coloured entries are explained in the text (page 30). The highest number of counts is observed for "green" bins in each ring R, followed by "blue" and "yellow" bins.

R	Type	"Green"	"Yellow"	"Orange"	"Blue"	"Violet"
1	Counts:	27	3	0	15	0
	Mean Deviation (%):	(0.162±0.04)	(0.19±0.03)	0	(0.140±0.05)	0
	Max Deviation (%):	(0.4±0.2)	(0.3±0.3)	0	(0.4±0.3)	0
2	Counts:	32	7	0	6	0
	Mean Deviation (%):	(0.17±0.02)	(0.14±0.01)	0	(0.14±0.04)	0
	Max Deviation (%):	(0.4±0.2)	(0.2±0.2)	0	(0.3±0.2)	0
3	Counts:	34	4	0	6	1
	Mean Deviation (%):	(0.18±0.02)	(0.16±0.02)	0	(0.16±0.03)	(0.3±0.1)
	Max Deviation (%):	(0.5±0.1)	(0.2±0.1)	0	(0.3±0.1)	(0.3±0.1)
4	Counts:	32	7	0	5	1
	Mean Deviation (%):	(0.23±0.03)	(0.13±0.02)	0	(0.13±0.03)	(0.3±0.1)
	Max Deviation (%):	(0.7±0.1)	(0.2±0.1)	0	(0.3±0.1)	(0.3±0.1)
5	Counts:	32	6	1	6	0
	Mean Deviation (%):	(0.26±0.04)	(0.28±0.08)	(0.75±0.09)	(0.07±0.02)	0
	Max Deviation (%):	(1.08±0.09)	(0.36±0.09)	(0.75±0.09)	(0.17±0.09)	0
6	Counts:	30	5	7	6	1
	Mean Deviation (%):	(0.96±0.08)	(0.22±0.01)	(0.8±0.2)	(0.08±0.04)	(0.2±0.1)
	Max Deviation (%):	(2.68±0.09)	(0.25±0.09)	(1.83±0.09)	(0.13±0.09)	(0.2±0.1)

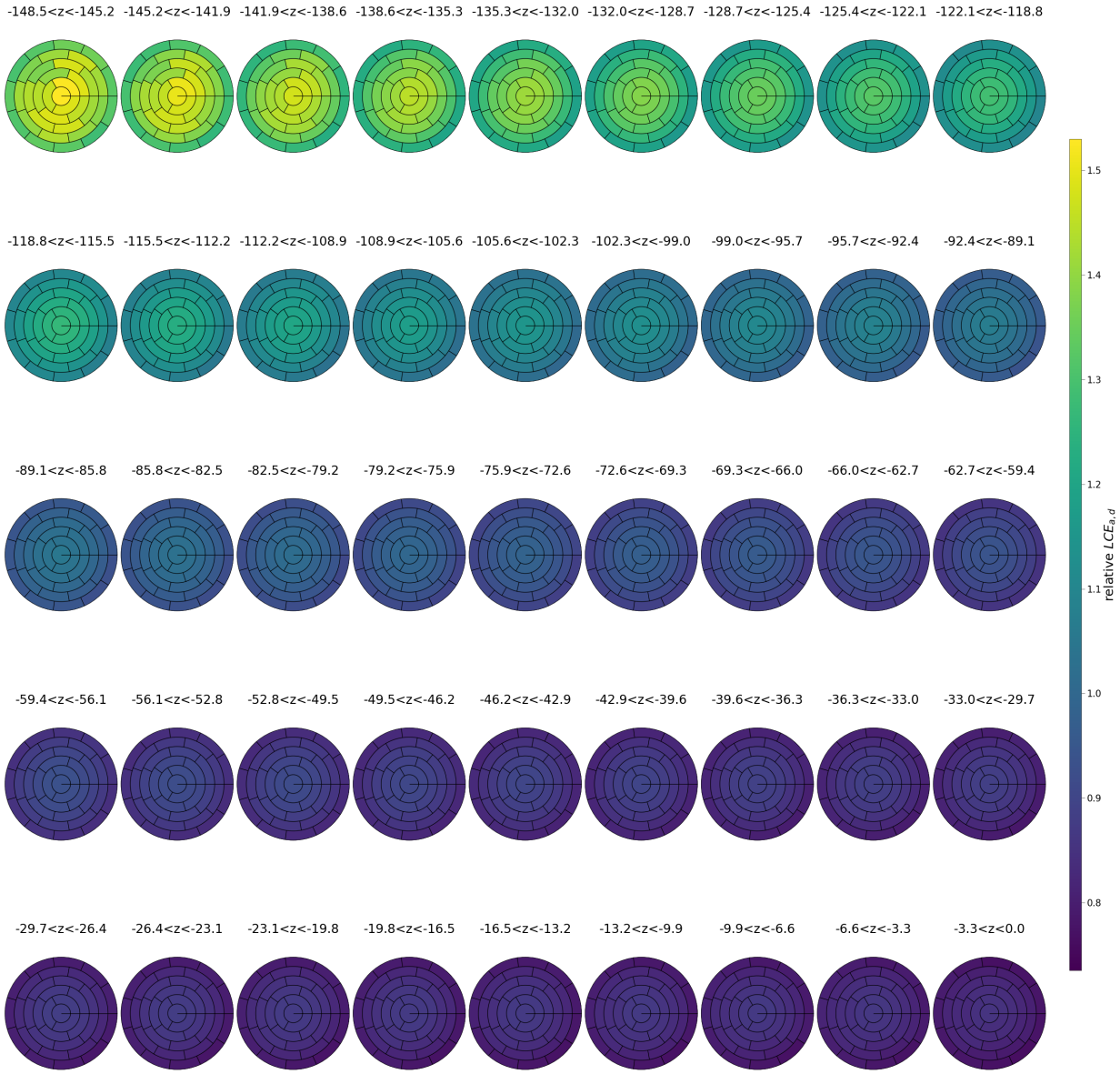

Figure A.1: Uncorrected relative LCE map of $S1_{a,d}$ for all bins in the TPC. The color bar indicates the relative light collection efficiency and the titles show the coordinates of each z-slice in cm. For increasing z the relative LCE decreases. A similar effect can be seen for increasing radii.

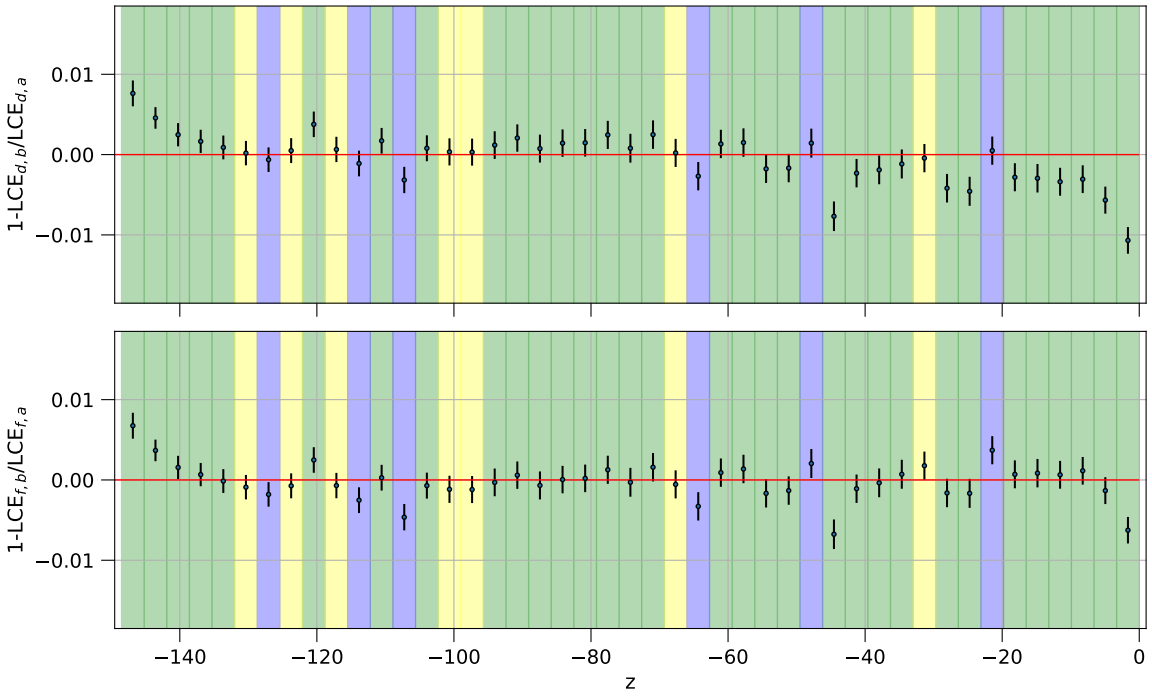

Figure A.2: For the ring between 11.1 cm and 22.2 cm the α and β are plotted against z. The colors of the shaded regions are explained in the text (page 30). Mainly "green" bins can be observed for this ring. The effect of N increases for increasing z.

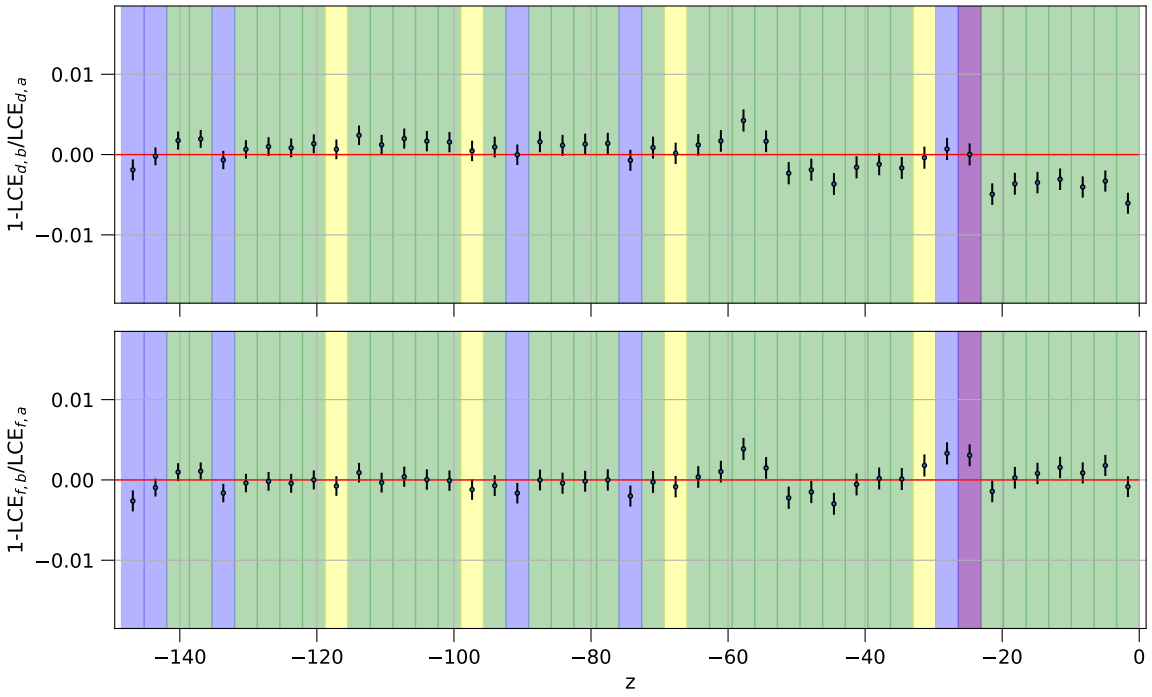

Figure A.3: For the ring between 22.2 cm and 33.2 cm the α and β are plotted against z. The colors of the shaded regions are explained in the text (page 30). For $z = -25$ cm a "violet" bin can be observed.

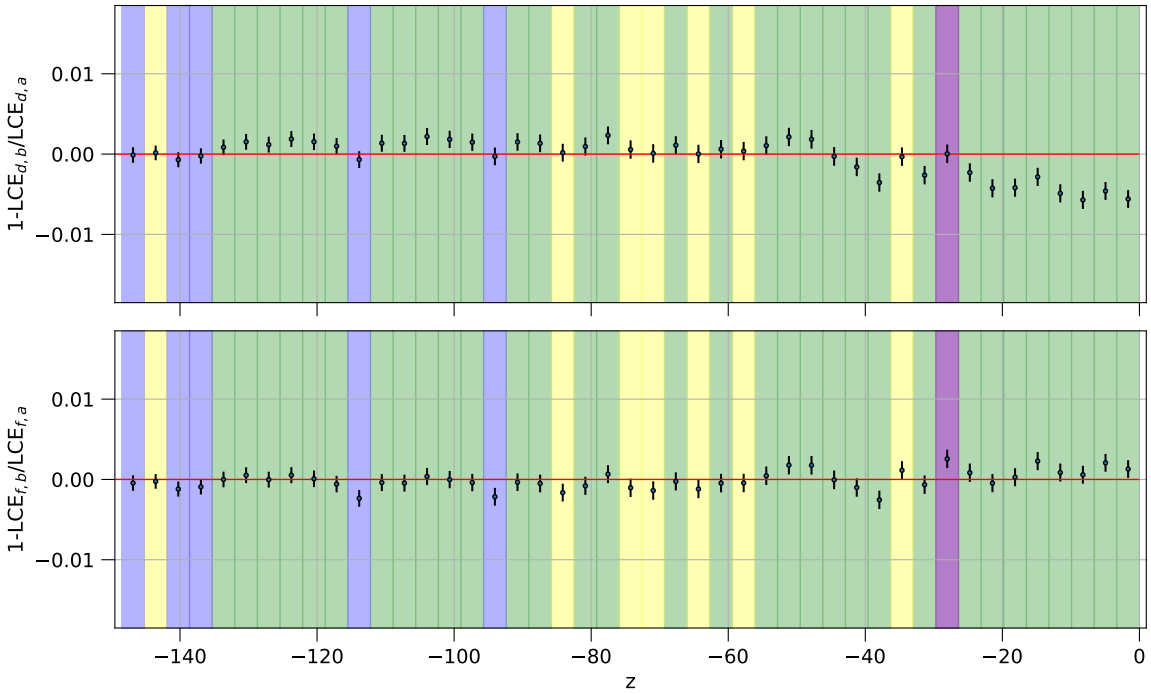

Figure A.4: For the ring between 33.2 cm and 44.3 cm the α and β are plotted against z. The colors of the shaded regions are explained in the text (page 30). For $z = -28$ cm a "violet" bin can be observed.

Bibliography

[1] COMSOL multiphysics. URL: https://www.comsol.com/. 13

[2] J.R. Angevaare et al. XENONnT/straxen: v1.7.2. July 2022. doi:10.5281/zenodo.6881647. 10

[3] E. Aprile and T. Doke. Liquid xenon detectors for particle physics and astrophysics. *Reviews of Modern Physics*, 82(3):2053–2097, Jul 2010. URL: https://doi.org/10.1103%2Frevmodphys.82.2053, doi:10.1103/revmodphys.82.2053. 4, 6, 25

[4] E. Aprile et al. Measurement of the scintillation yield of low-energy electrons in liquid xenon. *Physical Review D*, 86(11):112004, 2012. 19

[5] E. Aprile et al. The XENON1T dark matter experiment. *The European Physical Journal C*, 77(12):881, Dec 2017. doi:10.1140/epjc/s10052-017-5326-3. 4, 7, 10

[6] E. Aprile et al. XENON1T dark matter data analysis: Signal reconstruction, calibration, and event selection. *Phys. Rev. D*, 100:052014, Sep 2019. URL: https://link.aps.org/doi/10.1103/PhysRevD.100.052014, doi:10.1103/PhysRevD.100.052014. 6, 7

[7] E. Aprile et al. Projected WIMP sensitivity of the XENONnT dark matter experiment. *Journal of Cosmology and Astroparticle Physics*, 2020(11):031–031, Nov 2020. URL: https://doi.org/10.1088%2F1475-7516%2F2020%2F11%2F031, doi:10.1088/1475-7516/2020/11/031. 6

[8] E. Aprile et al. Search for new physics in electronic recoil data from XENONnT. *Physical Review Letters*, 129(16):161805, 2022. 5, 7, 13, 17

[9] K.G. Begeman et al. Extended rotation curves of spiral galaxies: dark haloes and modified dynamics. *Monthly Notices of the Royal Astronomical Society*, 249(3):523–537, Apr 1991. arXiv:https://academic.oup.com/mnras/article-pdf/249/3/523/18160929/mnras249-0523.pdf, doi:10.1093/mnras/249.3.523. 4

[10] G. Bertone et al. Particle dark matter: evidence, candidates and constraints. *Physics Reports*, 405(5):279–390, 2005. URL: https://www.sciencedirect.com/science/article/pii/S0370157304003515, doi:https://doi.org/10.1016/j.physrep.2004.08.031. 3

[11] P. Di Gangi. The XENON road to direct detection of dark matter at LNGS: The XENON project. *Universe*, 7(8), 2021. URL: https://www.mdpi.com/2218-1997/7/8/313, doi:10.3390/universe7080313. 4, 5

[12] T. Doke et al. LET dependence of scintillation yields in liquid argon. *Nuclear Instruments and Methods in Physics Research Section A: Accelerators, Spectrometers, Detectors and Associated Equipment*, 269(1):291–296, 1988. 16

[13] T. Doke et al. Absolute scintillation yields in liquid argon and xenon for various particles. *Japanese journal of applied physics*, 41(3R):1538, 2002. 16

[14] M. Erdmann and T. Hebbeker. Experimentalphysik 5: Moderne Methoden der Datenanalyse Physik Denken. *Springer*, 2013. 12

[15] H. Dembinski et al. scikit-hep/iminuit. Dec 2020. doi:10.5281/zenodo.3949207. 12

[16] L. Althüser for the XENON Collaboration. Nov 2022. URL: https://xe1t-wiki.lngs.infn.it/doku.php?id=xenon:xenonnt:althueser. 5

[17] C. Liebenthal. XENONnT and Kr-83m calibration REU program at Columbia University-Nevis Labs. 2022. 9

[18] B. Ostrick. Eine kondensierte 83mKr-Kalibrationsquelle für das KATRIN-Experiment. *Westfälische Wilhelms-Universität Münster*, 2009. 10

[19] R. Peres. 3D electric field simulations for XENONnT. 2020. URL: https://indico.phys.ethz.ch/event/20/contributions/91/attachments/78/104/3D_Electric_Field_Simulation_PhD_Seminar.pdf. 13

[20] P. Sorensen and C.E. Dahl. Nuclear recoil energy scale in liquid xenon with application to the direct detection of dark matter. *Physical Review D*, 83(6):063501, 2011. 16

[21] M. Szydagis et al. NEST: a comprehensive model for scintillation yield in liquid xenon, Oct 2011. URL: https://doi.org/10.1088%2F1748-0221%2F6%2F10%2Fp10002, doi:10.1088/1748-0221/6/10/p10002. 15, 16, 17, 20

[22] M. Szydagis et al. A review of basic energy reconstruction techniques in liquid xenon and argon detectors for dark matter and neutrino physics using NEST. *Instruments*, 5(1), 2021. URL: https://www.mdpi.com/2410-390X/5/1/13, doi:10.3390/instruments5010013. 18

[23] T. Takahashi et al. Average energy expended per ion pair in liquid xenon. *Physical Review A*, 12(5):1771, 1975. 16

[24] J. Thomas and D. A. Imel. Recombination of electron-ion pairs in liquid argon and liquid xenon. *Phys. Rev. A*, 36:614–616, Jul 1987. URL: https://link.aps.org/doi/10.1103/PhysRevA.36.614, doi:10.1103/PhysRevA.36.614. 16